Title

Toxicological Profiling of Metal Oxide Nanoparticles in Liver Context Reveals Pyroptosis in Kupffer Cells and Macrophages versus Apoptosis in Hepatocytes

Journal

ACS Nano, 12(4)

ISSN

1936-0851

Authors

Mirshafiee, Vahid
Sun, Bingbing
Chang, Chong Hyun
et al.

Publication Date

2018-04-24

DOI

10.1021/acsnano.8b01086

Peer reviewed

HHS Public Access

Author manuscript

ACS Nano. Author manuscript; available in PMC 2019 April 24.

Published in final edited form as:

ACS Nano. 2018 April 24; 12(4): 3836–3852. doi:10.1021/acsnano.8b01086.

Toxicological Profiling of Metal Oxide Nanoparticles in Liver Context Reveals Pyroptosis in Kupffer Cells and Macrophages *Versus* Apoptosis in Hepatocytes

Vahid Mirshafiee[†,‡,#], **Bingbing Sun**[‖,‡,#], **Chong Hyun Chang**[†], **Yu Pei Liao**[‡], **Wen Jiang**[†], **Jinhong Jiang**[†], **Xiangsheng Liu**[‡], **Xiang Wang**[†], **Tian Xia**[†,‡,*], and **André E. Nel**[†,‡,*]

[†]Center for Environmental Implications of Nanotechnology, California NanoSystems Institute, University of California Los Angeles, 570 Westwood Plaza, Los Angeles, California 90095, United States

[‡]Division of NanoMedicine, Department of Medicine, University of California Los Angeles, 10833 Le Conte Ave., Los Angeles, California 90095, United States

[‖]State Key Laboratory of Fine Chemicals, Department of Chemical Engineering, Dalian University of Technology, 2 Linggong Rd., Dalian 116024, China

Abstract

The liver and the mononuclear phagocyte system (MPS) is a frequent target for engineered nanomaterials (ENMs), either as a result of particle uptake and spread from primary exposure sites or systemic administration of therapeutic and imaging nanoparticles. In this study, we performed a comparative analysis of the toxicological impact of 29 metal oxide (MOx) nanoparticles (NPs), some commonly used in consumer products, in transformed or primary Kupffer cells (KCs) and hepatocytes. Not only did we observe differences between KC and hepatocytes, but also differences in the toxicological profiles of transition metal oxides (TMOs, *e.g.*, Co_3O_4) *versus* rare earth oxide (REO) NPs (*e.g.*, Gd_2O_3). While pro-oxidative TMOs induced the activation of caspases 3 and 7, resulting in apoptotic cell death in both cell types, REOs induced lysosomal damage, NLRP3 inflammasome activation, caspase 1 activation and pyroptosis in KCs. Pyroptosis was accompanied by cell swelling, membrane blebbing, IL-1β release, and increased membrane permeability, which could be reversed by knockdown of the pore forming protein, gasdermin D. Though similar features were not seen in hepatocytes, the investigation of the cytotoxic effects of REO NPs could also be seen to affect macrophage cell lines such as J774A.1 and RAW 264.7 cells, as well as bone marrow-derived macrophages (BMDMs). These phagocytic cell types also demonstrated features of pyroptosis and increased IL-1β production. Collectively, these findings demonstrate important mechanistic considerations that can be used for safety evaluation of metal oxides, including commercial products that are developed from these materials.

Graphical abstract

[*]Address correspondence to: txia@ucla.edu; anel@mednet.ucla.edu.
[#]These authors contributed equally to this work

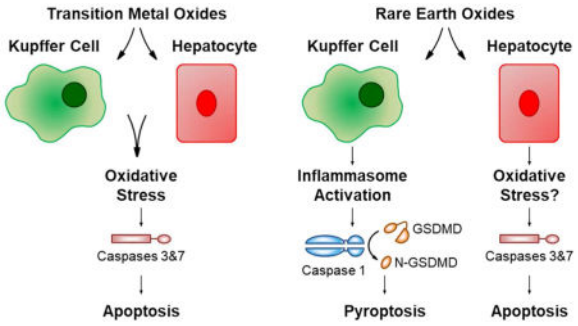

Keywords

Metal oxides; Kupffer cells; Hepatocytes; Macrophages; NLRP3 activation; Caspase 1; Pyroptosis

Metal oxide (MOx) nanoparticles are among the most abundant engineered nanomaterials (ENMs) that are produced worldwide for use in consumer products such as dietary supplements, cosmetics, fuel additives, personal care products and clothing.[1] In addition, transition MOx nanoparticles such as magnetic iron oxide (Fe_3O_4) or silicon dioxide (SiO_2), as well as rare earth oxides (REOs) such as gadolinium contrast agents, are widely used for therapeutic or diagnostic applications, including targeted drug delivery and magnetic resonance imaging (MRI). These widely used industrial and theranostic applications increase the possibility of human exposure to MOx nanomaterials. Previous studies for model MOx nanoparticles, including TiO_2 and europium-doped gadolinium oxide nanoparticles, have shown that following deposition of MOx nanoparticles in the lung and gastrointestinal (GI) tract, there is a high possibility of these materials translocating to the systemic circulation, with the potential to target secondary organs such as the mononuclear phagocyte system (MPS) and the liver.[2, 3] Furthermore, systemic administration of therapeutic or diagnostic MOx nanoparticles often results in significant bioaccumulation in the liver and the possibility of nanoparticle interactions with hepatic cells.[4] It is important, therefore, to develop safety screening methods for the assessment of MOx nanoparticle interactions with phagocytic cells and hepatocytes in the liver.

Nanoparticles are primarily phagocytosed by Kupffer cells (KCs) in the liver. These phagocytic cells, which reside in liver sinusoids, constitute 80-90% of tissue macrophages in the body.[4, 5] KCs play a key role in phagocytosis of foreign materials, endotoxin removal, and modulation of innate immune responses.[5, 6] Cellular uptake of MOx nanoparticles by KCs and the subsequent activation of these phagocytic cells could also impact hepatocytes, which primarily performs metabolic and detoxification functions such as synthesis and storage of carbohydrates and fatty acids, production of circulatory proteins and enzymes, and conjugation and excretion of toxic chemical substances. Activated KCs also produce reactive oxygen species and inflammatory mediators (*e.g.*, TNF-α, IL-1β, and IL-6) that affect hepatocyte function, including DNA synthesis and cytochrome P-450 activity.[7] Moreover, the production of these pro-inflammatory products by stimulated KCs induce an acute phase response in hepatocytes.[7] It is therefore important to mechanistically understand how MOx nanoparticles interact with these primary liver cell populations, and investigate

possible adverse effects as a result of these interactions. To date, few studies have addressed the hazard potential of MOx nanoparticles in the liver, and we also lack an understanding of the dose-response relationships, leading to adverse outcome. For example, Hussain *et al.* studied hepatotoxicity of Fe_3O_4, TiO_2, MoO_3, and MnO nanoparticles, using the rat liver fibroblast cell line, BRL 3A, demonstrating toxicological effects at high exposure doses (100-250 μg/mL).[8] Kermanizadeh *et al.* demonstrated that TiO_2 and ZnO nanoparticles induced toxicity in human hepatoblastoma C3A cells, in part, as a result of the generation of oxidative stress.[9] While these studies demonstrate hazard potential of a limited number of MOx nanoparticles, no comprehensive toxicological profiling has been undertaken for the various metal oxide categories, including their relationship to pathways of toxicity in cell types, such as Kupffer cells and hepatocytes.

In order to bridge this knowledge gap, we selected an extensive array of metal oxide nanoparticles, including transition metal oxides (TMOs, *e.g.*, Al_2O_3, Co_3O_4, MnO_2) and rare earth oxides (REOs, *e.g.*, Gd_2O_3, La_2O_3, Y_2O_3) to conduct comprehensive toxicological profiling of these materials in primary and transformed KCs, hepatocytes and macrophages. We combined two libraries of previously characterized TMOs and REOs, which were supplemented with five additional REO nanoparticles to comprise a comprehensive library of 29 nanomaterials. This material library was used to study the impact on cell viability and pro-inflammatory responses in KCs and hepatocytes. We demonstrate that while redox-active transition MOx nanoparticles display similar toxicological responses in KC and hepatocyte cell types, REOs induce differential toxicity in these cell types premised on subcellular processing and engagement of an injury response pathway that culminates in pyroptosis. We demonstrate that the REO-induced pyroptotic cell death pathway can also be engaged in macrophage cell lines, murine bone marrow-derived macrophages (BMDMs) and primary human KCs. No study of similar magnitude has ever been undertaken for the profiling of mechanistic injury responses in liver cell types, which significantly extends our understanding of metal oxide toxicity in this organ.

Results

Physical Characterization of Metal Oxide Nanoparticles

Previous toxicological profiling of two MOx nanoparticle libraries in the lung have shown the importance of toxic metal ion release from the soluble nanoparticles (*e.g.*, CuO and ZnO), the contribution of conduction band energy in the generation of reactive oxygen species by TMOs (*e.g.*, Co_3O_4 and Mn_2O_3), and the biotransformation of REOs (*e.g.*, Gd_2O_3 and La_2O_3) as a consequence of the complexation of biological phosphate groups in membranes and proteins.[10, 11] The grouping and mechanistic profiling of this comprehensive group of 24 materials are explained in the legend of Figure 1A. This library of nanomaterials was supplemented with 5 additional REOs (Dy_2O_3, Er_2O_3, Eu_2O_3, Nd_2O_3, and Sm_2O_3) for toxicological studies in KCs and hepatocytes. These are the primary liver cell types targeted by nanoparticle spread from primary exposure sites such as the GI tract or systemic biodistribution following intravenous administration (*e.g.*, imaging agents). While most materials were from commercial sources, Co_3O_4, CuO, Fe_3O_4, Sb_2O_3, TiO_2, WO_3, and ZnO were prepared in-house by flame spray pyrolysis (Table S1, Supporting Information). All the

nanoparticles were thoroughly characterized for crystal structure, primary size, hydrodynamic diameter and surface charge (Table S1, Supporting Information). The crystallinity information for each metal oxide nanoparticle was obtained by X-ray diffraction (XRD) analysis (Table S1, Supporting Information). Transition electron microscopy (TEM) was used to assess primary particle sizes (Figure 1B), which varied from 10 to 140 nm, except for Cr_2O_3 that was ~190 nm (Table S1, Supporting Information).[10, 11] While pristine REOs displayed spherical or irregular TEM shapes (Figure 1B), these materials transformed into urchin-shaped or mesh-like structures in the presence of phagolysosomal fluid, as a consequence of the release of the rare earth ions that bind to phosphates that subsequently precipitate on the particle surfaces (Figure 1C). The only exception is CeO_2, which displays extremely low solubility in acidic fluid as a result of its high thermodynamic stability.[12]

Nanoparticle characterization in aqueous and cell culture media showed that the majority of the nanoparticles formed large aggregates with hydrodynamic sizes of 200-1000 nm, except for Fe_3O_4 and WO_3, which formed aggregates of 150 nm and 120 nm, respectively (Table S1, Supporting Information). Most particles exhibited a positive zeta potential in deionized (DI) water, except Cr_2O_3, Fe_3O_4, Mn_2O_3, Sb_2O_3, SiO_2, SnO_2, WO_3, and ZrO_2, which displayed negative charges (Table S1, Supporting Information). The surface charge changed to a negative zeta potential of minus 9-15 mV in the presence of cell culture media, likely as a result of the formation of a protein corona (Table S1, Supporting Information).

Determination of MOx Toxicity in Hepatocytes and KCs

Hepatocytes and KCs are differentially impacted by toxic chemicals, drugs and particulate materials as a result of differences in cellular processing, uptake and physiological functions.[4] To perform toxicological profiling, we have selected representative hepatocyte (Hepa 1-6) and Kupffer cell lines (KUP5) to study the impact of the MOx nanoparticles in our library. The comparative analysis to primary KCs and hepatocytes will be described later. The first toxicological analysis was assessment of cell viability by the MTS assay. Without more details about real-life exposure in the liver, unlike pulmonary toxicity studies that can be related to ambient exposure concentrations, we selected a wide range of particle concentrations (6.25-200 μg/mL) for toxicological profiling, which can be used in future studies for reconciliation to *in vivo* exposure levels. This dose range is compatible with the concentrations used for individual or small batches of metal oxides to study hepatocyte toxicity.[8, 9, 13, 14] Following cellular exposure to the MOx nanoparticles, we could discern three response profiles related to particle composition. While REOs (except CeO_2 and Yb_2O_3) and redox-active/soluble TMOs exhibited relatively similar degree of toxicity in KUP5 cells, materials regarded as “inert TMOs” had no effect (Figure 2A). In contrast, REOs had significantly less toxicity in Hepa 1-6 compared to the KUP5 cells, while the TMOs, with the exception of Co_3O_4 and In_2O_3, exerted roughly similar toxicological effects as in KUP5 cells, with distinguishable differences between soluble/redox-active and “inert” materials (Figure 2B). The heat maps in Figures 2C and 2D provide a visual display of the response profiles of KCs and hepatocytes, in addition to depicting the increased susceptibility of KCs to the REOs. In contrast, the responses to TMOs were more similar. These differences could reflect differences in cellular uptake and triggering of death response pathways.

MOx Nanoparticles Induce Differential Cell Death Responses in KUP5 and Hepa 1-6 Cells

We used optical microscopy to observe the morphology of dying KUP5 and Hepa 1-6 cells in response to particle exposure (Figure 3A and Figures S1-S2, Supporting Information). The introduction of most REOs (*e.g.*, Gd_2O_3 and Y_2O_3, but not CeO_2) in KUP5 cells was accompanied by significant cell swelling and the appearance of giant surface blebs (Figure 3A and Figure S1, Supporting Information). The cellular response culminated in surface membrane rupture and release of intracellular content (Video S1, Supporting Information). The same necrotic cell death features were not observed in REO-treated Hepa 1-6 cells (Figure S2, Supporting Information). In contrast to REOs, incubation of KUP5 cells with Co_3O_4, Mn_2O_3, and ZnO particles resulted in cellular shrinking, nuclear condensation, and nuclear fragmentation (Figure 3A and Figure S1, Supporting Information), which represent features of apoptotic cell death.[15] Similar features were not observed with TiO_2 nanoparticles, which is in keeping with lack of an effect on KUP5 cell viability (Figure 3A). These morphological features suggest that there are variances in triggering of cell death responses by the different nanomaterial categories.

In order to assess the mechanisms of cell death, Annexin V-FITC and propidium iodide (PI) staining was used to compare different particles during the performance of flow cytometry. This demonstrated that REO exposure to KUP5 cells show increased PI staining without an increase in Annexin V surface staining (Figure 3B). This is compatible with a non-apoptotic cell death mechanism. In contrast, Co_3O_4 and Mn_2O_3 exposure induced increased Annexin V plus PI staining in KUP5 cells, which is consistent with apoptotic cell death (Figure 3B). Hepa 1-6 cells showed positive staining for both Annexin V and PI in response to all of the materials (except Co_3O_4), indicating that in this cell type redox-active TMOs and REOs are capable of inducing apoptosis (Figure 3B). These data provide further proof of differences in the mechanisms of cell death.

In order to more specifically delineate the cell death mechanisms in KUP5 and Hepa 1-6 cells, confocal microscopy was used to assess caspase activation profiles that reflect apoptotic and non-apoptotic death.[16] In this context, it is known that caspases 3 and 7 are executioner proteases during cellular apoptosis,[16] while caspase 1 activation has been linked to cell death responses that are accompanied by lysosome damage and activation of the NLRP3 inflammasome.[17] REO nanoparticles can trigger lysosomal damage by complexing the structural phosphate groups from phospholipids in the lysosomal membrane.[11] Confocal assessment of the caspase activation was performed in both cell types during treatment with 50 μg/mL CeO_2, Gd_2O_3, La_2O_3, Y_2O_3, Co_3O_4, and Mn_2O_3 nanoparticles for 3 h. The activation of caspase 1 was assessed by using the FAM-FLICA® Caspase-1 substrate, FAM-YVAD-FMK, while the FAM-FLICA® Caspase-3/7 substrate, FAM-DEVD-FMK, was used to assess activation of caspases 3 and 7 (Figure 4). The results demonstrated the activation of caspase 1 by Gd_2O_3, La_2O_3, and Y_2O_3 in KUP5 cells but not by CeO_2, Co_3O_4, and Mn_2O_3 nanoparticles (Figure 4A). In contrast, no caspase 1 staining was detected in Hepa 1-6 cells for any of the materials (Figure 4A). Caspases 3 and 7 staining showed robust activation of these proteases in KUP5 and Hepa 1-6 cells by Gd_2O_3, La_2O_3, Y_2O_3, and Mn_2O_3 particles, while CeO_2 and Co_3O_4 had a less prominent outcome (Figure 4B). These results demonstrate that while REOs (with the exception of CeO_2) trigger caspase 1 activation in

KUP5 cells, this is not the case in Hepa 1-6 cells. However, a range of REO and TMO nanoparticles could activate caspases 3 and 7 in both cell types. The effect of REOs on the activation of these caspases was confirmed by western blotting (Figure S3, Supporting Information). It has been demonstrated that caspases 3 and 7 can be activated downstream of caspase 1.[18] Collectively, these data suggest differential mechanisms of subcellular processing and uptake that leads to the engagement of specific cell death pathways.

Subcellular Localization and Differential Lysosomal Damage and Inflammasome Activation by MOx Nanoparticles

To assess nanoparticle uptake, processing and possible differences in lysosome damage in KUP5 and Hepa 1-6 cells, inductively coupled plasma optical emission spectrometry (ICP-OES), TEM, and confocal microcopy were used following cellular exposure to CeO_2, Gd_2O_3, La_2O_3, Y_2O_3, Co_3O_4, and Mn_2O_3 nanoparticles. ICP-OES analysis of metal content in KUP5 and Hepa 1-6 cells showed that there were no significant differences in the cellular content of Ce, Gd, La, and Co between cells, while the uptake of Y_2O_3 and Mn_2O_3 nanoparticles was higher in hepatocytes than KCs (Figure 5A). Use of confocal microscopy in both cell types to demonstrate the subcellular localization of DyLight 594-labeled CeO_2, Gd_2O_3, Y_2O_3, and TiO_2 nanoparticles in relation to the LAMP-1 stained lysosomal compartment, demonstrated that the majority (60 to 80%) of labeled nanoparticles co-localized with Alexa 488-labeled LAMP-1 antibody, as assessed by ImageJ software (Figure 5B, C). TEM images of KUP5 and Hepa 1-6 cells exposed to CeO_2, Gd_2O_3, La_2O_3, Y_2O_3, Co_3O_4, and Mn_2O_3 nanoparticles confirmed their cellular uptake in both cell types, in addition to demonstrating the transformation of Gd_2O_3, La_2O_3, Y_2O_3 (but not CeO_2) nanoparticles into urchin or mesh-like structures within intracellular vesicles (Figure 5D, E). Interestingly, the biotransformed particles were localized in proximity to the membranes of the giant vesicles forming in KUP5 cells, but not seen in Hepa 1-6 cells (Figure 5D, E).

In order to assess lysosome integrity, we used the detection of a Magic Red-labeled cathepsin B substrate for confocal microscopy. These images demonstrate that the punctate staining pattern of the intact lysosomes in non-exposed KUP5 cells disappeared upon exposure to Gd_2O_3, La_2O_3, and Y_2O_3 particles (Figure 6A). This can be explained by cathepsin B release into the cytosol, followed by leakage from the cell, as a result of surface membrane damage. No effect was observed on the integrity of the lysosomes in KUP5 cells treated with CeO_2, Co_3O_4 and Mn_2O_3 (Figure 6A). Interestingly, the punctate Magic Red staining profile was maintained in Hepa 1-6 cells for all the particles, suggesting absence of lysosomal damage (Figure 6A). In order to confirm this, we made use of our previous demonstration that lysosomal damage and cathepsin B release is known to trigger NLRP3 inflammasome activation and IL-1β production in macrophage cell lines.[17, 19, 20, 21, 22] Measurement of IL-1β release into the supernatants of MOx-treated KUP5 cells showed significant cytokine production in response to Gd_2O_3, La_2O_3, and Y_2O_3, but not CeO_2 or Co_3O_4 nanoparticles (Figure 6B). This is consistent with the confocal data. Moreover, the inclusion of a cathepsin B inhibitor, CA-074-ME, during cellular exposure demonstrated a decrease in IL-1β production in response to Gd_2O_3, La_2O_3, and Y_2O_3 (Figure 6B). Screening of IL-1β production in KUP5 cells exposed to all MOx nanoparticles showed significant inflammatory responses for REOs, but no significant increase in IL-1β

production by other particle types (Figure 6C). The role of the NLRP3 inflammasome in IL-1β production was confirmed by knockdown of the NLRP3 component, as demonstrated in (Figure S4 Supporting Information). Interestingly, no increase in IL-1β production could be seen in hepatocytes in response to particle exposure (Figure 6D), which could be ascribed to failure of pro-IL-1β production in response to LPS treatment (Figure 6E). A possible explanation for lysosomal damage in KUP5 but not Hepa 1-6 cells could be differences in the levels of acidification in the phagolysosomes of phagocytic cells *vs.* the lysosomes of hepatocytes.[23] According to the literature, the lysosomal pH of phagocytic cells is 5-5.5, while the pH of hepatocyte lysosomes are closer to 6.5.[23] In order to confirm this notion, we assessed the dissolution of REOs for 30 min over a range of pH levels. The results are presented in Figure 6F, which demonstrates that while all particles underwent dissolution, there was a clear difference for CeO_2 in relation to the other REOs. The data demonstrate clear pH-dependent dissolution for Gd_2O_3 and La_2O_3 particles, which is accentuated in the pH 5.5-6.5 range, corresponding to the lysosomal pH differences mentioned above.[23]

REO Nanoparticles Induce Pyroptosis in KUP5 Cells

The induction of cellular swelling, giant blebbing, caspase 1 activation and IL-1β production in KUP5 cells is suggestive of a form of cell death known as pyroptosis (Figure 7A). Pyroptosis is classically used as a cell death response in the setting of infectious disease agents such as Salmonella and Shigella, where macrophage cell death contributes to intense IL-1β-mediated inflammation, as well as the release of the pro-inflammatory cellular content as a consequence of pore formation in the surface membrane and leakage.[15, 24, 25] The formation of these pores is dependent on gasdermin D (GSDMD), which is a substrate for activated caspase 1, leading to the release of the N-terminal fragment from the auto-inhibitory C-terminal domain.[18, 26, 27, 28, 29, 30, 31, 32, 33] These N-terminal fragments translocate to the cell membrane, where their oligomerization leads to pore formation. This disturbs ion and water flux across the membrane, leading to cellular swelling, formation of membrane blebbing, and leakage and release of the intracellular content (Figure 7A). In order to confirm the role of GSDMD in REO-induced pyroptosis, siRNA knockdown of GSDMD was performed during assessment of LDH release from KUP5 cells treated with CeO_2, Gd_2O_3, La_2O_3, Y_2O_3, Co_3O_4 and nigericin (positive control) (Figure 7B). This demonstrated a reduction in cytosolic enzyme release from REO-exposed cells in which GSDMD was knocked down compared to wild type cells or cells treated with scrambled (negative control) siRNA.

REOs Induce Pyroptosis in Primary KCs and Other Macrophages, but Not Hepatocytes

In order to demonstrate the relevance of the cellular responses studied in transformed cell lines in primary cell types, a limited number of studies were performed in primary KCs, bone marrow-derived macrophages (BMDMs) and other macrophage cell lines (Figure 8). While treatment with CeO_2, Gd_2O_3, La_2O_3, Y_2O_3, and Co_3O_4 nanoparticles resulted in cell viability reduction in primary KCs (Figure 8A), only Gd_2O_3, La_2O_3, and Y_2O_3 increased the production of IL-1β (Figure 8B). Moreover, the macrophage cell lines, J774A.1 and Raw 264.7 cells, as well as BMDMs showed similar response profiles as primary KC and KUP5 cells (Figure 8C). Additionally, REO-treated macrophages responded with increased IL-1β production (Figure 8D) and demonstrated a dose-dependent inflammatory response (Figure

S5, Supporting Information). Optical microscopy demonstrated morphological features of pyroptosis, similar to KUP5 cells (Figure 8E). In contrast to the macrophages, primary hepatocytes exhibited no pyroptotic features or increased IL-1β production, in spite of the significant reduction in cell viability (Figure S6, Supporting Information). These data suggest the induction of pyroptosis in macrophages and Kupffer cells as a specific feature of phagocytic cells in response to REO nanoparticles.

Discussion

In this article, we performed toxicological profiling of 29 rare earth and transition metal oxide nanoparticles in Kupffer cells and hepatocytes to determine the impact on cellular viability and pro-inflammatory effects, based on MOx class, cellular uptake, subcellular localization, lysosome damage, and triggering of cell death response pathways. Even though REOs are taken up in both KUP5 and Hepa 1-6 cells, only the former cell type undergoes pyroptosis, as demonstrated by cell swelling, development of giant membrane blebs, caspase 1 activation, IL-1β production and LDH release, which could be suppressed by gasdermin D knockdown. Interestingly, although REO nanoparticles co-localized with the LAMP-1 positive compartment in both cell types, only KUP5 cells showed signs of lysosomal damage, leading to the recruitment and activation of caspase 1 to the NLRP3 inflammasome, where it induces pro-IL-1β cleavage. This response could be suppressed by a cathepsin B inhibitor. In contrast, REOs (with the exception of CeO_2) and redox-active TMOs could trigger caspase 3 and caspase 7 activation in Hepa 1-6 cells, which developed features of apoptotic cell death, without evidence of caspase 1 activation or IL-1β production. Moreover, a number of biologically inert TMOs failed to exert any cytotoxic effects in either cell type. The contrasting features of KUP5 and Hepa 1-6 cells were reduplicated in primary KCs and hepatocytes. Moreover, we also demonstrated that other phagocytic cell types, including bone marrow-derived macrophages and macrophage cell lines, exhibit features of pyroptosis in response to REOs (other than CeO_2). The lack of response to CeO_2 can be explained by its reduced rate of dissolution under acidifying conditions as a result of its thermodynamic stability.[12] These data may be of considerable importance for the screening and analysis of the potentially hazardous effects of metal oxide nanoparticles in the liver.

The most important finding in the current study is the distinct toxicological response profiles of KCs and hepatocytes in terms of the response to the different metal oxide categories. KCs are one of the major components of the MPS, and constitute 15% of all liver cells or 80-90% of all tissue macrophages in the body.[34] KCs performs a janitorial function that protects hepatocytes by removal of cellular debris and foreign materials through the process of phagocytosis and phagolysosomal digestion.[4] Within this process, KCs could release substances that require hepatocyte uptake and metabolism,[7] which could potentially lead to the induction of pro-inflammatory responses in hepatocytes through the release of TNF-α, IL-6 and IL-1β.[7] Moreover, KCs also regulate and maintain hepatocyte detoxification, including conjugation and metabolic conversion of chemicals by cytochrome P450 enzymes.[7, 35] The cross-communication between KCs and hepatocytes is likely also important during the encounter of the liver to the metal oxides. Moreover, there are a variety of toxicity pathways that could lead to adverse outcome in the liver based on the composition and properties of MOx nanoparticles and the corresponding effects on KCs and hepatocytes. In

this regard, we have previously demonstrated during predictive toxicological studies in the lung that highly soluble TMOs, redox-active TMOs, catalytically inert TMOs and REOs induce cell-specific effects in epithelial cells and macrophages, which translate into acute and chronic adverse outcomes in this organ.[10, 11, 36]

It was possible to discern three major cell viability response profiles in KUP5 and Hepa 1-6 cells, dependent on material composition. While most REOs, with the exception of CeO_2, induce cytotoxic effects in both cell types, the decline in cell viability was generally more prominent in KUP5 than in Hepa 1-6 cells (Figure 2). Moreover, there was a difference in the mechanism of cell death, which was characterized as pyroptosis in the KC cell line and apoptosis in Hepa 1-6 cells (Figures 3, 4 and 7). The induction of pyroptosis by the REOs was characterized by typical morphological features of cell blebbing, NLRP3 inflammasome activation, IL-1β production, and the involvement of gasdermin D (Figure 7). An interesting question therefore becomes why KCs and hepatocytes react differently, because REOs (with the exception of CeO_2) undergo biotransformation to urchin-shaped structures in both cell types (Figure 5D, E). The morphological change is the result of the release of rare earth (RE) ions from the particle surface at acidic pH, leading to the complexation and capture of biological phosphates from cellular membranes and proteins. These complexes precipitate as $REPO_4$ crystals on the particle surface (Figure 1A, C).[11] The biotransformation triggers the lysosomal damage, cathepsin B release and NLRP3 assembly in KUP5 cells (Figure 6). This leads to caspase 1 recruitment, and cleavage of pro-IL-1β (Figure 6). IL-1β is involved in the pyroptosis pathway, and its cellular levels in phagocytic cells can be further boosted by interference in autophagy flux as we have previously demonstrated in the study of REOs in THP-1 cells.[37] In spite of the intracellular biotransformation of REOs in hepatocytes, these cells did not demonstrate evidence of lysosome damage, caspase 1 activation and IL-1β production (Figures 4, 5 and 6). While the exact explanation for this difference in cellular behavior is unknown, we have already referred to the differences in the level of lysosomal acidification in macrophages *vs.* hepatocytes (Figure 6F).[23] Moreover, triggering of the V-ATPase that is responsible for lysosomal acidification in macrophages could lead to the import of protons, followed by counter ions (Cl^-) and water molecules.[38] This osmotic effect could ultimately be responsible for swelling of the lysosome and rupture to release their content in KUP5, but not Hepa 1-6 cells. The notion of a macrophage-specific injury response is also in keeping with our demonstration that REOs could also induce pyroptosis features in other macrophage cell lines, and in bone marrow-derived macrophages (Figure 8). While intracellular LPS has been shown to induce pyroptosis in non-phagocytic murine cells by a pathway that involves caspase 11,[30, 39] we did not observe evidence of pyroptotic cell death in Hepa 1-6 cells.

A second form of cell death (apoptosis) in response to TMOs has previously been shown by us to involve ROS generation and oxidative stress.[10, 40] This effect was confirmed in the current study by the decrease in intracellular GSH levels in KUP5 and Hepa 1-6 cells, following exposure to TMOs (Figure S7, Supporting Information). From a mechanistic perspective, this involves at least two major molecular initiating events that can lead to oxidative stress. The 1st is the shedding of Cu^{2+} and Zn^{2+} by CuO and ZnO nanoparticles after cellular uptake. These metal ions generate ROS through a variety of different mechanisms, leading to the generation of a tier 2 oxidative stress response, which can trigger

the activation of pro-inflammatory cytokines and chemokines, as we have previously demonstrated.[10, 40] Tier 2 oxidative stress is accompanied by activation of the NF-κB and AP-1 transcriptional pathways.[41] More intense oxidative stress can also trigger a tier 3 toxic oxidative stress response, which leads to apoptotic cell death as a result of perturbation of the mitochondrial PT pore and release of cytochrome c.[10, 40] In this regard; the response profiles of CuO and ZnO in KCs and hepatocytes were equivalent, demonstrating an apoptosis response (Figure 2). This is in agreement with the work of Kermanizadeh *et al.*, who demonstrated that the generation of oxidative stress by ZnO nanoparticles was associated with cytotoxicity in a human hepatoblastoma cell line.[9] Further analysis of ZnO nanoparticle toxicity in human hepatocytes revealed that oxidative stress and lipid peroxidation played a critical role in ZnO-induced cell membrane disruption, DNA damage, and cell death.[42] The second major pathway of TMO-induced oxidative stress is linked to the conduction bandgap of CoO, Co_3O_4, Mn_2O_3, and Ni_2O_3, which are known to function as p-type semiconductors.[10] It has also subsequently been shown by PdO-doping of Co_3O_4 nanoparticles that the Fermi level accompanying the band gap bending plays a role.[43] We have previously demonstrated that the conduction band energy of these materials, which correspond to −4.18 to −4.82 eV on the absolute vacuum scale, can participate in electron transfer to and from surrounding cellular redox couples that contribute to the establishment of a cellular redox potential.[10] The electron exchange triggers ROS production, which in accordance to the severity, can culminate in antioxidant defense (tier 1), pro-inflammatory effects (tier 2) and cell death (tier 3).[38, 41, 44] We demonstrate roughly equivalent responses in KUP5 and Hepa 1-6 cells, as shown in Figures 2 and S7 (Supporting Information). These findings are consistent with previous studies that found liver toxicity for cobalt, manganese, and nickel nanoparticles.[8, 45, 46] Liu *et al.* also reported that exposure of BRL 3A rat derived liver cells to Co nanoparticles reduced cell viability and LDH release, which was accompanied by ROS generation and DNA damage.[45] Similar induction of LDH release was found for micron-size MnO_2 particles in the same liver cell line.[8] For nickel (Ni) nanoparticles, it was shown that their deposition into the rat liver after intravenous administration caused histopathological changes and significant alteration in the serum levels of bilirubin and alkaline phosphatase (ALP).[46] In addition to the redox-active TMOs that involve ROS generation as a result of surface electronic properties, we also observed that In_2O_3 and Sb_2O_3 particles exert cytotoxic effects (Figure 2). Although there are no reports with regard to the liver toxicity of indium (In) and antimony (Sb) nanoparticles as far as we could ascertain, hepatotoxicity has been reported as a side-effect of Sb-containing compounds for the treatment of leishmaniasis, based on glutathione depletion and ROS production.[47] Further studies may be required to look into the possibility that In_2O_3 and Sb_2O_3 nanoparticles may lead to hepatotoxicity, based on our cellular studies.

The third response outcome was the failure to observe cytotoxicity by TMOs that are regarded as catalytically inert (Figure 2). The apparent inert status of aluminum (Al), iron oxide (Fe_3O_4), titanium dioxide (TiO_2), and tungsten (W) nanoparticles was also previously demonstrated in the BRL 3A rat liver cell line.[8] Moreover, incubation of C3A liver hepatocytes with TiO_2 nanoparticles did not affect metabolic functions such as gluconeogenesis and glycogenolysis; this was attributed to the lack of an effect on ROS production and oxidative stress.[48] Furthermore, there was no evidence of ROS generation or

interference in mitochondrial function for these particles.[10, 48] However, in spite of our attempts to demonstrate cytotoxic effects in KCs and hepatocytes, this does not imply that these materials are devoid of hazard potential. For instance, TiO_2 nanoparticles are capable of becoming catalytically active upon ultraviolet (UV) exposure, leading to the formation of electron hole pairs that can catalyze oxidative stress effects.[49] In addition, titanium dioxide nanoparticles exist as anatase or rutile crystalline forms, which can affect their photocatalytic activity, and possibly cytotoxicity.[48, 50] Therefore, the exposure scenario and material composition could lead to hazard potential of so-called catalytically inert TMOs. For example, it has been shown that while single-dose exposure of SiO_2 nanoparticles failed to induce profibrogenic effects in the murine lungs, repetitive dosing of the same material may induce particle retention in the lung and subchronic lung injury.[51] Another example is paramagnetic iron oxide nanoparticles, which are generally considered safe for MRI, but could contribute to iron overload, iron-induced oxidative stress and lipid peroxidation in cirrhosis patients, with disease exacerbation.[52, 53]

Our study demonstrates toxicological profiling of an extensive range of metal oxide nanoparticles in KCs and hepatocytes, premised on mechanistic injury responses. Because of the comprehensive nature of the current study and coverage of a large number of nanomaterials in terms of their mechanistic injury responses, our *in vitro* data will enable us to construct molecular initiating events (Figure 1A), key events and key event relationships that can be used to plan limited, but informative animal studies. These planned *in vivo* experiments will include the use of transgenic animals, which express reporter genes linked to the mechanisms of injury, as well as performing *ex vivo* tissue analysis, *e.g.*, cell sorting. The integrated process could lead to the development of adverse outcome pathways (AOPs), which can be used for toxicological profiling of any newly introduced MOx nanoparticle. An AOP knowledge base could also provide a reference grid against which new materials can be assessed by well-established and simple-to-perform toxicological assays that are derived from the key events. The hazard assessment could also be used for tiered risk assessment and decision making whether to perform *in vivo* testing.

Another utility of our assessment approach is to use the data related to molecular initiating events to construct structure-activity relationships that can be used for safer material design. For instance, the toxicity associated with the biotransformation of REOs can be reduced by surface coating with organo-phosphonates, which can prevent particle dissolution and the complexation of biological phosphates.[11] In this regard, we have demonstrated that phosphonate coating of rare earth containing imaging (upconversion) nanoparticles can improve material safety and avoid the equivalence scenario of Gd-containing contrast agents inducing systemic nephrogenic fibrosis.[54] Another example, relevant to the pulmonary toxicity of ZnO and CuO nanoparticles, is that particle doping can decrease the dissolution rate that is important for the generation of acute pro-inflammatory effects in the lung.[36, 55]

Conclusion

The toxicological profiling of 29 metal oxide nanoparticles in Kupffer cells, macrophages and hepatocytes, demonstrate that redox-active and highly soluble TMOs (*e.g.*, Mn_2O_3, CuO, and ZnO), as well as rare earth oxides (*e.g.*, Gd_2O_3, La_2O_3, and Y_2O_3), except CeO_2,

are the most toxic metal oxides in the liver cells. While rare earth oxides induce pyroptosis in the former two cell types, the same impact was not seen in hepatocytes. In contrast, the redox-active TMOs induce apoptosis in both KCs and hepatocytes. The generation of pyroptosis in KCs and macrophages by REOs is premised on triggering of lysosomal damage and NLRP3 inflammasome activation. Our study provides a reference grid for toxicity screening of metal oxides, which can help to establish a knowledge base for the safety assessment and risk analysis.

Methods

Reagents and Materials

We have previously described the commercial acquisition and in-house synthesis of 24 different metal oxide nanoparticles.[10] The particle library was increased to 29 materials by the acquisition of Dy_2O_3, Er_2O_3, Eu_2O_3, and Sm_2O_3 from US Research Nanomaterials, Inc., and Nd_2O_3 from Nanostructured & Amorphous Materials, Inc. (See Table S1, Supporting Information). The CellTiter 96® AQueous MTS Assay, GSH-Glo™ Glutathione Assay, and CytoTox 96® NonRadioactive Cytotoxicity (LDH) Assay kits were purchased from Promega (Madison, WI). The Annexin V-FITC Apoptosis Detection Kit and rat anti-mouse monoclonal LAMP-1 antibody were purchased from Abcam (Cambridge, MA). The FAM-FLICA® Caspase-1, Caspase-3/7, and Magic Red Cathepsin B Assay Kits were purchased from ImmunoChemistry Technologies, LLC (Bloomington, MN). Rabbit anti-mouse monoclonal antibody recognizing cleaved caspase 3 and rabbit anti-mouse polyclonal antibody recognizing cleaved caspase 7 were purchased from Cell Signaling Technology, Inc. (Danvers, MA). The cathepsin B inhibitor, CA-074-Me, lipopolysaccharide (LPS) and GSDMD, NLRP3 and caspase 1 siRNAs were obtained from Sigma (St. Louis, MO). The ELISA kits for human and mouse IL-1β were purchased from R&D Systems (Minneapolis, MN) and BD Biosciences (San Diego, CA), respectively. The DyLight™ 594 NHS Ester, ELISA kits for mouse IL-1β pro-form and primary human Kupffer cells were purchased from Thermo Fisher Scientific (Waltham, MA). The mouse Kupffer cell line, KUP5, was purchased from RIKEN CELL BANK (Japan). The hepatocyte cell line, Hepa 1-6, was purchased from ATCC, and the primary mouse hepatocytes were provided by Lonza (Walkersville, MD). The mouse macrophage cell lines, J774A.1 and RAW 264.7, were purchased from Sigma (St. Louis, MO).

Physical Characterizations of MOx Nanoparticles

The particles were characterized as received without further purification or modification. Their morphologies and primary sizes were assessed by TEM (JEOL 1200 EX transmission electron microscope). The crystallinity information was obtained by performing X-ray diffraction (XRD) using a Panalytical X'Pert Pro diffractometer with a 2θ range of 10°-80° and equipped with Cu Kα radiation. The For particle characterization in suspension, the stock solutions were prepared at a concentration of 1 mg/mL in filtered deionized (DI) water, followed by sonication for 15 min in a water bath sonicator. These suspensions were then diluted in DI water or cell culture media to final concentrations of 50 μg/mL, followed by further sonication for 15 min. The hydrodynamic diameters and zeta (ζ) potentials of particles in DI water and DMEM were determined using a ZetaPALS instrument

(Brookhaven Instrument, Holtsville, NY). Transformation of REOs in PSF fluid was performed following the previously reported procedure.[11] Briefly, the nanoparticles were dispersed in PSF buffer containing Na_2HPO_4, NaCl, Na_2SO_4, $CaCl_2{\bullet}H_2O$, glycine, and potassium phthalate by sonication, followed by 24 h incubation at 37 °C. Next, the particles were collected and thoroughly washed with deionized water before their morphology was characterized by TEM.

Cell Culture

KUP5 cells were grown in high glucose DMEM media supplemented with 10% fetal bovine serum (FBS), 10 μg/mL bovine insulin and 250 μM 1-Thioglycerol. Hepa 1-6, J774A.1 and RAW 264.7 cells were grown in high glucose DMEM media supplemented with 10% FBS and 100 U/mL-100 μg/mL penicillin-streptomycin. Bone marrow-derived macrophages (BMDMs) were cultured in 25% LADMAC (mouse bone marrow, producing colony stimulating factor-1) conditioned medium and maintained in high glucose DMEM media supplemented with 10% FBS before use.[22] Primary human Kupffer cells were maintained in RPMI 1640 media supplemented with GlutaMAX™-I, 25 mM HEPES, 10% FBS and 100 U/mL-100 μg/mL penicillin-streptomycin. Primary mouse hepatocytes were maintained in Hepatocyte Maintenance Medium (Lonza).

Isolation and Preparation of BMDMs

The bone marrow of female C57BL/6 mice were used to prepare BMDMs according to our previously described procedure.[56] Briefly, femurs and tibia were cut on both ends and the marrow cavity carefully washed with DMEM. The cells were passed through a 70-μm cell strainer, followed by centrifugation at 400 g for 10 min at 4 °C and re-suspension in 1 mL of ice-cold 25% LADMAC-conditioned medium. The cells were plated (1×10^6 cells/mL) in 100 mm petri dishes in the same medium and grown at 37 °C and 5% CO_2 for seven days, while replacing the media every two days. Cells were re-plated at 5×10^4 cells/well in complete DMEM medium in a 96-well plate. The established BMDMs were treated with recombinant murine IFN-γ (10 ng/mL) for 48 h prior to use.

Assessment of Nanoparticle Cytotoxicity

The viability of KUP5, Hepa 1-6, J774A.1, and RAW 264.7 cells, as well as BMDMs, primary Kupffer cells, and primary hepatocytes were assessed by the MTS assay. Cells were exposed to the nanoparticles at the indicated concentrations for 24 h in a 96-well plate, followed by removal of the medium and replacement with 120 μL of complete cell culture media containing 16.7% of a MTS stock solution for 1 h at 37 °C. The plates were centrifuged at 2000*g* for 10 min in an Eppendorf 5430 microcentrifuge with microplate rotor to collect the cell debris and nanoparticles. Subsequently, 100 μL supernatant was removed from each well and transferred into a new 96-well plate. The absorbance was read at 490 nm on a SpectraMax M5e microplate reader (Molecular Devices, Sunnyvale, CA). Cytotoxic damage to the cell membrane in wild type and siRNA-transfected KUP5 cells was also assessed by using the CytoTox 96 Non-Radioactive Cytotoxicity Assay to measure LDH release. Following exposure to nanoparticles at 200 μg/mL in a 96-well plate, 50 μL of each cell supernatant was mixed with 50 μL of reconstituted Substrate Mix, and incubated at room temperature for 30 min. Next, 50 μL of Stop Solution was added to each well and the

absorbance was read at 490 nm on a SpectraMax M5e microplate reader (Molecular Devices, Sunnyvale, CA).

Assessment of Pyroptotic Cell Death under Optical Microscopy

Optical microscopy was used to monitor the morphology of KUP5 cells, pretreated with 1 μg/mL LPS for 4 h, during exposure to 12.5 μg/ml nanoparticles for 6 h at 37 °C and 5% CO_2 in an 8-well Lab-Tek® chamber slide. The cells were examined using a Zeiss Optical Microscope. In order to monitor the time kinetics of the pyroptosis event in LPS pre-treated cells, 10×10^4 KUP5 cells/mL were exposed to 50 μg/ml Gd_2O_3 nanoparticles for 6 h in a 35 mm glass bottom dish (In Vitro Scientific) at 37 °C and 5% CO_2. Light optic images were obtained every two minutes under a Leica Confocal SP5 Blue microscope.

Determination of Apoptosis *via* Annexin-V Staining and Flow Cytometry

KUP5 and Hepa 1-6 cells were plated at a density of 8×10^5 cells per well in a 6-well plate overnight. The medium was replaced with fresh medium in the presence of LPS (1 μg/mL) and incubated for an additional 4 h. The primed KUP5 and Hepa 1-6 cells were treated with 200 μg/mL nanoparticles for 3 and 18 h, respectively. After collection of the cell pellets and supernatants, followed by washing in PBS, the Annexin V-FITC Apoptosis Detection Kit was used for cellular staining according to the manufacturer's procedure. The cells were analyzed with a BD LSR II Flow Cytometer by using FITC and PE channels for detection of Annexin V-FITC and PI staining, respectively. Finally, the flow cytometry results were analyzed with FCS Express 6 software to identify Annexin V/PI-positive cells as apoptotic populations and Annexin V-negative/PI-positive cells as populations undergoing non-apoptotic cell death.

Determination of Caspases 1 and 3&7 Activity by Confocal Microscopy and Western Blotting

KUP5 and Hepa 1-6 cells were cultured in an 8-well Lab-Tek® chamber slide at 5×10^4 cells/400 μL medium at 37 °C and 5% CO_2. The cells were primed with LPS (1 μg/mL) for 4 h, and incubated with nanoparticles at 50 μg/mL for 3 h. Cells were washed with PBS and stained with either FAM-FLICA® Caspase-1 or Caspase-3/7 substrates for 1 h at 37 °C following the manufacturer's procedure. Finally, the cells were fixed with 4% paraformaldehyde in PBS, stained with Hoechst 33342 (5 μg/mL) and imaged using Leica Confocal SP8-SMD microscope. For western blotting, KUP5 and Hepa 1-6 cells were plated overnight at a density of 8×10^5 cells per well in 6-well plates. The cells were primed with LPS (1 μg/mL) for 4 h, and then exposed to nanoparticles at 50 μg/mL for 3 h. The exposed cells were washed in PBS and lysed in lysis buffer containing a cocktail of protease inhibitors. The cellular extracts were separated on 10-20% SDS-polyacrylamide gel at 150 V and transferred to a PDVF membrane at 45 V. The blotting membranes were blocked with 5% milk in TBS/Tween 20 (0.2%) for 1 h at room temperature, and then incubated with primary antibody (1/1000 in blocking buffer), overnight at 4 °C. After washing three times with TBS/Tween 20 (0.1%) and addition of HRP-conjugated secondary antibody (1/1000 in blocking buffer) for 1 h at room temperature, membranes were washed three times with TBST/Tween 20 (0.1%) and developed with a freshly prepared luminol-based detection solution.

Determination of IL-1β Production

KUP5, Hepa 1-6, J774A.1 and RAW 264.7 cells in 100 μL of tissue culture medium were plated overnight at a density of 2×10^4 cells per well in a 96-well plate. The cells were primed by replacing the tissue culture medium with fresh medium containing 0.1 μg/mL LPS to treat the RAW 264.7 macrophage cell line or 1 μg/mL LPS to treat other cell types for 4 h. The primed cells were exposed to nanoparticles at the indicated concentrations and time periods as shown in each figure legend. For BMDMs, 5×10^4 cells were grown at 37 °C for 5 h in 100 μL tissue culture medium, supplemented with 500 ng/mL LPS. After replacement of the medium, the primed BMDMs were treated with nanoparticles at the indicated concentrations in the figure legend for 24 h, in the presence of 10 ng/mL LPS. The cellular supernatants were collected for IL-1β quantification. To assess the effect of cathepsin B inhibitor, KUP5 cells were treated with particles in the presence of cathepsin B inhibitor, CA-074-Me (30 μM), for 6 h. IL-1β production in primary Kupffer cells and hepatocytes were assessed by growing the cells in 100 μL tissue culture medium in 96 well plates, at a density of 3×10^4 per well and in the presence of 1 μg/mL LPS for 4 h. The medium was replaced with fresh media and the primed cells treated with ENMs (50 μg/mL) for 24 h. The supernatants were collected for IL-1β measurement.

Determination of pro-IL-1β Activity in LPS-primed Cells

KUP5 and Hepa 1-6 cells were plated overnight in 96-well plates at 2×10^4 cells per well. Following priming of the cells with 1 μg/mL LPS for 4 h, cells were lysed by using three freeze–thaw cycles in 100 μL lysis buffer (10 μM 2-ME, 9 mM $MgCl_2$ and 0.1% triton X-100 in DPBS). The cellular lysates were obtained after centrifugation and used for the quantification of pro-IL-1β by an ELISA (Thermo Fisher Scientific).

Assessment of Nanoparticle Uptake in Cells by ICP-OES

KUP5 and Hepa 1-6 cells in 1 mL of cell culture medium were plated overnight at a density of 8×10^5 cells per well in a 6-well plate. The cells were primed with LPS (1 μg/mL) for 4 h, and then exposed to nanoparticles at 12.5 μg/mL for 4 h. Particle-treated cells were collected from the plate and washed 3 times in PBS. Cells were lysed in 200 μL of lysis buffer (10 μM 2-ME, 9 mM $MgCl_2$ and 0.1% triton X-100 in DPBS) to assess the protein content of the supernatant, using a Bradford assay. Acid digestion was performed on cell lysates containing ~0.45 mg of cellular proteins by using 10 mL of a mixture of concentrated HNO_3 (65-70%, Trace Metal Grade, Fisher Scientific) and HCl (35-38%, Trace Metal Grade, Fisher Scientific) in a ratio of 1:3 at 95 °C for 2 days in a HotBlock (SC100, Environmental Express). Inductively coupled plasma optical emission spectrometry (ICP-OES) analysis was performed to determine the metal content. The metal content was quantified using an ICP-OES (ICPE-9000, Shimadzu, Japan), using triplicate analysis of each sample and standard in the presence of 2% (v/v) nitric acid. Digested cell culture media, which do not contain nanoparticles, served as the reagent blank.

Determining the Localization of Fluorescent-labeled ENMs in Lysosomes

Metal oxides were fluorescently labeled with DyLight 594 following the procedure reported previously.[40] Briefly, the nanoparticles were first reacted with aminopropyltriethoxysilane

(APTES) to introduce functional primary amine groups on their surfaces. Functionalized NPs were then incubated with DyLight™ 594 NHS Ester for fluorescence labeling. To study the possibility of lysosomal localization, KUP5 and Hepa 1-6 cells were cultured in an 8-well Lab-Tek® chamber slide at 5×10^4 cells/400 μL medium at 37 °C and 5% CO_2. Cells were primed with LPS (1 μg/mL) for 4 h, and exposed to 12.5 μg/mL of fluorescent-labeled particles for 2h, in the case of KUP5 cells, or 6 h for Hepa 1-6 cells. Cells were washed with PBS and LAMP-1 staining was performed as previously reported. Briefly, cells were fixed and permeabilized with 4% paraformaldehyde and 0.2% Triton X-100, respectively. Following blocking with 3% BSA solution for 1 h at room temperature, the permeabilized cells were incubated with primary rat anti-mouse LAMP-1 antibody (1:1000 dilution) overnight at 4 °C. This was followed by secondary staining with Alexa 488 conjugated goat anti-rat antibody (1:800 dilution) and cellular nuclear staining with Hoechst 33342 (5 μg/mL). Fluorescent images were acquired on a Leica Confocal SP8-SMD microscope. Co-localization of particles with LAMP-1 was determined by ImageJ software analysis.

Cellular TEM Analysis

KUP5 and Hepa 1-6 cells in 1 mL of tissue culture medium were plated at 8×10^5 cells per well in a 6-well plate, and cultured overnight. Cells were primed with LPS (1 μg/mL) for 4 h, and then exposed to 25 μg/mL nanoparticles for 2 h at 37 °C. Particle-treated cells were first washed with PBS, collected and washed again with a fixing solution containing 2.5% glutaraldehyde and 2% paraformaldehyde in PBS, followed by overnight incubation at 4 °C in fresh fixing solution. After post-fixation was performed in 1% OsO_4 in PBS for 1 h, the cells were dehydrated in a graded ethanol series. The procedure was completed by propylene oxide treatment, Epon embedding, sectioning, and placement on Formvar-coated copper grids. The sections were stained with uranyl acetate and Reynolds lead citrate. The images were obtained using a JEOL 1200 EX transmission electron microscope at 80 kV.

Assessment of Lysosomal Damage by Cathepsin B Staining

After KUP5 and Hepa 1-6 cells were cultured overnight in an 8-well Lab-Tek® chamber slide at 5×10^4 cells per well, the cells were primed with LPS (1 μg/mL) for 4 h and exposed to particles (50 μg/mL) for 1 h at 37 °C. The cells were washed with PBS and incubated with Magic Red working solution for 30 min at 37 °C. Cells were washed with PBS and fixed with 4% paraformaldehyde in PBS. Finally, the cells were stained with Hoechst 33342 (5 μg/mL), washed with PBS, and imaged under a Leica Confocal SP8-SMD microscope.

Determining Particle Dissolution at Different pH levels

Suspensions of CeO_2, Gd_2O_3, and La_2O_3 nanoparticles were prepared at 100 μg/mL in 1.5 mL of each four different MES buffers with the pH adjusted to 4.5, 5.5, 6.5, and 7.5. The suspensions were incubated at 37 °C for 30 min, followed by centrifugation at 15000 rpm for 10 min. The supernatants were collected and subjected to acid digestion by using 10 mL of a mixture of concentrated HNO_3 (65-70%, Trace Metal Grade, Fisher Scientific) and HCl (35-38%, Trace Metal Grade, Fisher Scientific) in a ratio of 1:3 at 95 °C for 2 days in a HotBlock (SC100, Environmental Express). ICP-OES analysis was performed to determine the metal content. The metal content was quantified by an ICP-OES (ICPE-9000, Shimadzu, Japan), using triplicate analysis of each sample and standard in the presence of 2% (v/v)

nitric acid. Digested MES buffers, which do not contain nanoparticles, served as the blank reagent.

Determining Intracellular GSH levels

The intracellular GSH level for KUP5 and Hepa 1-6 cells after nanoparticle treatment was assessed by the GSH-Glo™ Glutathione Assay. Cells were exposed to the nanoparticles at 50 μg/mL for 24 h in a 96-well plate, followed by removal of the medium and replacement with 100 μL of GSH-Glo™ reagent. After 30 min incubation, 100 μL of reconstituted luciferin detection reagent was added to the plate. Following 15 min incubation, luminescence was measured using a SpectraMax M5e microplate reader (Molecular Devices, Sunnyvale, CA).

siRNA Knockdown in KUP5 Cells

Knockdown of GSDMD, NLRP3 and caspase 1 genes were performed in KUP5 cells using electroporation at the Integrated Molecular Technologies Core Facility (University of California, Los Angeles). Briefly, 6 μg of siRNA in 100 μL media were electroporated into 1×10^6 KUP5 cells. After electroporation, cells were maintained in complete media for another 48 hours before cytotoxicity and IL-1β production analysis.

Supplementary Material

Refer to Web version on PubMed Central for supplementary material.

Acknowledgments

This work was supported by the National Institute of Environmental Health Sciences of the National Institutes of Health under the Award Number, R01 ES016746. The authors thank the CNSI Advanced Light Microscopy/ Spectroscopy and Electron Imaging Center for NanoMachines Core Facilities, the Flow Cytometry Core Facility of Jonsson Comprehensive Cancer Center, the Microscopic Techniques & Electron Microscope Core Facility of Brain Research Institute, and the Integrated Molecular Technologies Core (CURE/P30 DK041301) at UCLA. The authors would also like to thank Alex Andres, University of California Center for Environmental Implications of Nanotechnology, for the post-editing of the time-lapse video.

References

1. Vance ME, Kuiken T, Vejerano EP, McGinnis SP, Hochella MFJr, Rejeski D, Hull MS. Nanotechnology in the Real World: Redeveloping the Nanomaterial Consumer Products Inventory. Beilstein J Nanotechnol. 2015; 6:1769–80. [PubMed: 26425429]
2. Abid AD, Anderson DS, Das GK, Van Winkle LS, Kennedy IM. Novel Lanthanide-Labeled Metal Oxide Nanoparticles Improve the Measurement of *in Vivo* Clearance and Translocation. Part Fibre Toxicol. 2013; 10:1. [PubMed: 23305071]
3. Wang J, Zhou G, Chen C, Yu H, Wang T, Ma Y, Jia G, Gao Y, Li B, Sun J, Li Y, Jiao F, Zhao Y, Chai Z. Acute Toxicity and Biodistribution of Different Sized Titanium Dioxide Particles in Mice after Oral Administration. Toxicol Lett. 2007; 168:176–185. [PubMed: 17197136]
4. Zhang Y-N, Poon W, Tavares AJ, McGilvray ID, Chan WCW. Nanoparticle–Liver Interactions: Cellular Uptake and Hepatobiliary Elimination. J Controlled Release. 2016; 240:332–348.
5. Harbrecht BG, Billiar TR. The Role of Nitric Oxide in Kupffer Cell-Hepatocyte Interactions. Shock. 1995; 3:79–87. [PubMed: 7538434]
6. Zinchenko YS, Culberson CR, Coger RN. Contribution of Non-Parenchymal Cells to the Performance of Micropatterned Hepatocytes. Tissue Eng. 2006; 12:2241–1251. [PubMed: 16968164]

7. Billiar TR, Curran RD. Kupffer Cell and Hepatocyte Interactions: A Brief Overview. J Parenter Enteral Nutr. 1990; 14:175S–180S.
8. Hussain SM, Hess KL, Gearhart JM, Geiss KT, Schlager JJ. *In Vitro* Toxicity of Nanoparticles in BRL 3A Rat Liver Cells. Toxicol In Vitro. 2005; 19:975–983. [PubMed: 16125895]
9. Kermanizadeh A, Gaiser BK, Hutchison GR, Stone V. An *in Vitro* Liver Model - Assessing Oxidative Stress and Genotoxicity Following Exposure of Hepatocytes to a Panel of Engineered Nanomaterials. Part Fibre Toxicol. 2012; 9:28. [PubMed: 22812506]
10. Zhang H, Ji Z, Xia T, Meng H, Low-Kam C, Liu R, Pokhrel S, Lin S, Wang X, Liao Y-P, Wang M, Li L, Rallo R, Damoiseaux R, Telesca D, Mädler L, Cohen Y, Zink JI, Nel AE. Use of Metal Oxide Nanoparticle Band Gap to Develop a Predictive Paradigm for Oxidative Stress and Acute Pulmonary Inflammation. ACS Nano. 2012; 6:4349–4368. [PubMed: 22502734]
11. Li R, Ji Z, Chang CH, Dunphy DR, Cai X, Meng H, Zhang H, Sun B, Wang X, Dong J, Lin S, Wang M, Liao Y-P, Brinker CJ, Nel A, Xia T. Surface Interactions with Compartmentalized Cellular Phosphates Explain Rare Earth Oxide Nanoparticle Hazard and Provide Opportunities for Safer Design. ACS Nano. 2014; 8:1771–1783. [PubMed: 24417322]
12. Plakhova TV, Romanchuk AY, Yakunin SN, Dumas T, Demir S, Wang S, Minasian SG, Shuh DK, Tyliszczak T, Shiryaev AA, Egorov AV, Ivanov VK, Kalmykov SN. Solubility of Nanocrystalline Cerium Dioxide: Experimental Data and Thermodynamic Modeling. J Phys Chem C. 2016; 120:22615–22626.
13. Liu Y, Chen Z, Wang J. Systematic Evaluation of Biocompatibility of Magnetic Fe_3O_4 Nanoparticles with Six Different Mammalian Cell Lines. J Nanopart Res. 2011; 13:199–212.
14. Zhang L, Wang X, Zou J, Liu Y, Wang J. Effects of an 11-nm DMSA-Coated Iron Nanoparticle on the Gene Expression Profile of Two Human Cell Lines, THP-1 and HepG2. J Nanobiotechnology. 2015; 13:3. [PubMed: 25595381]
15. Bergsbaken T, Fink SL, Cookson BT. Pyroptosis: Host Cell Death and Inflammation. Nat Rev Microbiol. 2009; 7:99–109. [PubMed: 19148178]
16. McIlwain DR, Berger T, Mak TW. Caspase Functions in Cell Death and Disease. Cold Spring Harb Perspect Biol. 2013; 5:a008656. [PubMed: 23545416]
17. Szabo G, Csak T. Inflammasomes in Liver Diseases. J Hepatol. 2012; 57:642–654. [PubMed: 22634126]
18. Taabazuing CY, Okondo MC, Bachovchin DA. Pyroptosis and Apoptosis Pathways Engage in Bidirectional Crosstalk in Monocytes and Macrophages. Cell Chem Biol. 2017; 24:507–514.e4. [PubMed: 28392147]
19. Wang X, Xia T, Duch MC, Ji Z, Zhang H, Li R, Sun B, Lin S, Meng H, Liao Y-P, Wang M, Song T-B, Yang Y, Hersam MC, Nel AE. Pluronic F108 Coating Decreases the Lung Fibrosis Potential of Multiwall Carbon Nanotubes by Reducing Lysosomal Injury. Nano Lett. 2012; 12:3050–3061. [PubMed: 22546002]
20. Duewell P, Kono H, Rayner KJ, Sirois CM, Vladimer G, Bauernfeind FG, Abela GS, Franchi L, Nunez G, Schnurr M, Espevik T, Lien E, Fitzgerald KA, Rock KL, Moore KJ, Wright SD, Hornung V, Latz E. NLRP3 Inflammasomes Are Required for Atherogenesis and Activated by Cholesterol Crystals. Nature. 2010; 464:1357–1361. [PubMed: 20428172]
21. Duncan JA, Gao X, Huang MT-H, O'Connor BP, Thomas CE, Willingham SB, Bergstralh DT, Jarvis GA, Sparling PF, Ting JPY. Neisseria Gonorrhoeae Activates the Proteinase Cathepsin B to Mediate the Signaling Activities of the NLRP3 and ASC-Containing Inflammasome. J Immunol. 2009; 182:6460–6469. [PubMed: 19414800]
22. Sun B, Wang X, Ji Z, Wang M, Liao Y-P, Chang CH, Li R, Zhang H, Nel AE, Xia T. NADPH Oxidase-Dependent NLRP3 Inflammasome Activation and Its Important Role in Lung Fibrosis by Multiwalled Carbon Nanotubes. Small. 2015; 11:2087–2097. [PubMed: 25581126]
23. Sun B, Tran KK, Shen H. Enabling Customization of Non-Viral Gene Delivery Systems for Individual Cell Types by Surface-Induced Mineralization. Biomaterials. 2009; 30:6386–6393. [PubMed: 19695695]
24. Cunha LD, Zamboni DS. Subversion of Inflammasome Activation and Pyroptosis by Pathogenic Bacteria. Front Cell Infect Microbiol. 2013; 3:76. [PubMed: 24324933]

25. Fink SL, Cookson BT. Pyroptosis and Host Cell Death Responses During Salmonella Infection. Cell Microbiol. 2007; 9:2562–2570. [PubMed: 17714514]
26. He, W-t, Wan, H., Hu, L., Chen, P., Wang, X., Huang, Z., Yang, Z-H., Zhong, C-Q., Han, J. Gasdermin D Is an Executor of Pyroptosis and Required for Interleukin-1β Secretion. Cell Res. 2015; 25:1285–1298. [PubMed: 26611636]
27. Kayagaki N, Stowe IB, Lee BL, O/'Rourke K, Anderson K, Warming S, Cuellar T, Haley B, Roose-Girma M, Phung QT, Liu PS, Lill JR, Li H, Wu J, Kummerfeld S, Zhang J, Lee WP, Snipas SJ, Salvesen GS, Morris LX, et al. Caspase-11 Cleaves Gasdermin D for Non-Canonical Inflammasome Signalling. Nature. 2015; 526:666–671. [PubMed: 26375259]
28. Liu X, Zhang Z, Ruan J, Pan Y, Magupalli VG, Wu H, Lieberman J. Inflammasome-Activated Gasdermin D Causes Pyroptosis by Forming Membrane Pores. Nature. 2016; 535:153–158. [PubMed: 27383986]
29. Sborgi L, Rühl S, Mulvihill E, Pipercevic J, Heilig R, Stahlberg H, Farady CJ, Müller DJ, Broz P, Hiller S. GSDMD Membrane Pore Formation Constitutes the Mechanism of Pyroptotic Cell Death. EMBO J. 2016; 35:1766–1778. [PubMed: 27418190]
30. Shi J, Gao W, Shao F. Pyroptosis: Gasdermin-Mediated Programmed Necrotic Cell Death. Trends Biochem Sci. 2017; 42:245–254. [PubMed: 27932073]
31. Shi J, Zhao Y, Wang K, Shi X, Wang Y, Huang H, Zhuang Y, Cai T, Wang F, Shao F. Cleavage of GSDMD by Inflammatory Caspases Determines Pyroptotic Cell Death. Nature. 2015; 526:660–665. [PubMed: 26375003]
32. Vande Walle L, Lamkanfi M. Pyroptosis. Curr Biol. 2016; 26:R568–R572. [PubMed: 27404251]
33. Aglietti RA, Estevez A, Gupta A, Ramirez MG, Liu PS, Kayagaki N, Ciferri C, Dixit VM, Dueber EC. Gsdmd P30 Elicited by Caspase-11 During Pyroptosis Forms Pores in Membranes. Proc Natl Acad Sci U S A. 2016; 113:7858–7863. [PubMed: 27339137]
34. Sitia G, Iannacone M, Aiolfi R, Isogawa M, van Rooijen N, Scozzesi C, Bianchi ME, von Andrian UH, Chisari FV, Guidotti LG. Kupffer Cells Hasten Resolution of Liver Immunopathology in Mouse Models of Viral Hepatitis. PLoS Pathog. 2011; 7:e1002061. [PubMed: 21655107]
35. Peterson TC, Renton KW. Kupffer Cell Factor Mediated Depression of Hepatic Parenchymal Cell Cytochrome P-450. Biochem Pharmacol. 1986; 35:1491–1497. [PubMed: 2423090]
36. Xia T, Zhao Y, Sager T, George S, Pokhrel S, Li N, Schoenfeld D, Meng H, Lin S, Wang X, Wang M, Ji Z, Zink JI, Mädler L, Castranova V, Lin S, Nel AE. Decreased Dissolution of ZnO by Iron Doping Yields Nanoparticles with Reduced Toxicity in the Rodent Lung and Zebrafish Embryos. ACS Nano. 2011; 5:1223–1235. [PubMed: 21250651]
37. Li R, Ji Z, Qin H, Kang X, Sun B, Wang M, Chang CH, Wang X, Zhang H, Zou H, Nel AE, Xia T. Interference in Autophagosome Fusion by Rare Earth Nanoparticles Disrupts Autophagic Flux and Regulation of an Interleukin-1β Producing Inflammasome. ACS Nano. 2014; 8:10280–10292. [PubMed: 25251502]
38. Nel AE, Madler L, Velegol D, Xia T, Hoek EMV, Somasundaran P, Klaessig F, Castranova V, Thompson M. Understanding Biophysicochemical Interactions at the Nano-Bio Interface. Nat Mater. 2009; 8:543–557. [PubMed: 19525947]
39. Broz P. Immunology: Caspase Target Drives Pyroptosis. Nature. 2015; 526:642–643. [PubMed: 26375000]
40. Xia T, Kovochich M, Liong M, Mädler L, Gilbert B, Shi H, Yeh JI, Zink JI, Nel AE. Comparison of the Mechanism of Toxicity of Zinc Oxide and Cerium Oxide Nanoparticles Based on Dissolution and Oxidative Stress Properties. ACS Nano. 2008; 2:2121–2134. [PubMed: 19206459]
41. Nel A, Xia T, MadleL R, Li N. Toxic Potential of Materials at the Nanolevel. Science. 2006; 311:622–627. [PubMed: 16456071]
42. Guan R, Kang T, Lu F, Zhang Z, Shen H, Liu M. Cytotoxicity, Oxidative Stress, and Genotoxicity in Human Hepatocyte and Embryonic Kidney Cells Exposed to ZnO Nanoparticles. Nanoscale Res Lett. 2012; 7:602. [PubMed: 23110934]
43. Zhang H, Pokhrel S, Ji Z, Meng H, Wang X, Lin S, Chang CH, Li L, Li R, Sun B, Wang M, Liao Y-P, Liu R, Xia T, Mädler L, Nel AE. PdO Doping Tunes Band-Gap Energy Levels as Well as Oxidative Stress Responses to a Co_3O_4 P-Type Semiconductor in Cells and the Lung. J Am Chem Soc. 2014; 136:6406–6420. [PubMed: 24673286]

44. Meng H, Xia T, George S, Nel AE. A Predictive Toxicological Paradigm for the Safety Assessment of Nanomaterials. ACS Nano. 2009; 3:1620–1627. [PubMed: 21452863]
45. Liu YK, Deng XX, Yang HL. Cytotoxicity and Genotoxicity in Liver Cells Induced by Cobalt Nanoparticles and Ions. Bone Jt Res. 2016; 5:461–469.
46. Magaye RR, Yue X, Zou B, Shi H, Yu H, Liu K, Lin X, Xu J, Yang C, Wu A, Zhao J. Acute Toxicity of Nickel Nanoparticles in Rats after Intravenous Injection. Int J Nanomedicine. 2014; 9:1393–1402. [PubMed: 24648736]
47. Kato KC, Morais-Teixeira E, Reis PG, Silva-Barcellos NM, Salaün P, Campos PP, Dias Corrêa-Junior J, Rabello A, Demicheli C, Frézard F. Hepatotoxicity of Pentavalent Antimonial Drug: Possible Role of Residual Sb(III) and Protective Effect of Ascorbic Acid. Antimicrob Agents Chemother. 2014; 58:481–488. [PubMed: 24189251]
48. Filippi C, Pryde A, Cowan P, Lee T, Hayes P, Donaldson K, Plevris J, Stone V. Toxicology of ZnO and TiO_2 Nanoparticles on Hepatocytes: Impact on Metabolism and Bioenergetics. Nanotoxicology. 2015; 9:126–134. [PubMed: 24708275]
49. George S, Pokhrel S, Ji Z, Henderson BL, Xia T, Li L, Zink JI, Nel AE, Mädler L. Role of Fe Doping in Tuning the Band Gap of TiO_2 for the Photo-Oxidation-Induced Cytotoxicity Paradigm. J Am Chem Soc. 2011; 133:11270–11278. [PubMed: 21678906]
50. Karlsson HL, Cronholm P, Gustafsson J, Möller L. Copper Oxide Nanoparticles Are Highly Toxic: A Comparison between Metal Oxide Nanoparticles and Carbon Nanotubes. Chem Res Toxicol. 2008; 21:1726–1732. [PubMed: 18710264]
51. Sun B, Wang X, Liao Y-P, Ji Z, Chang CH, Pokhrel S, Ku J, Liu X, Wang M, Dunphy DR, Li R, Meng H, Mädler L, Brinker CJ, Nel AE, Xia T. Repetitive Dosing of Fumed Silica Leads to Profibrogenic Effects through Unique Structure–Activity Relationships and Biopersistence in the Lung. ACS Nano. 2016; 10:8054–8066. [PubMed: 27483033]
52. Wei Y, Zhao M, Yang F, Mao Y, Xie H, Zhou Q. Iron Overload by Superparamagnetic Iron Oxide Nanoparticles Is a High Risk Factor in Cirrhosis by a Systems Toxicology Assessment. Sci Rep. 2016; 6:29110. [PubMed: 27357559]
53. Zhou Q, Wei Y. For Better or Worse, Iron Overload by Superparamagnetic Iron Oxide Nanoparticles as a MRI Contrast Agent for Chronic Liver Diseases. Chem Res Toxicol. 2017; 30:73–80. [PubMed: 28092939]
54. Li R, Ji Z, Dong J, Chang CH, Wang X, Sun B, Wang M, Liao Y-P, Zink JI, Nel AE, Xia T. Enhancing the Imaging and Biosafety of Upconversion Nanoparticles through Phosphonate Coating. ACS Nano. 2015; 9:3293–3306. [PubMed: 25727446]
55. Naatz H, Lin S, Li R, Jiang W, Ji Z, Chang CH, Köser J, Thöming J, Xia T, Nel AE, Mädler L, Pokhrel S. Safe-by-Design CuO Nanoparticles Via Fe-Doping, Cu–O Bond Length Variation, and Biological Assessment in Cells and Zebrafish Embryos. ACS Nano. 2017; 11:501–515. [PubMed: 28026936]
56. Lin S, Wang X, Ji Z, Chang CH, Dong Y, Meng H, Liao Y-P, Wang M, Song T-B, Kohan S, Xia T, Zink JI, Lin S, Nel AE. Aspect Ratio Plays a Role in the Hazard Potential of CeO_2 Nanoparticles in Mouse Lung and Zebrafish Gastrointestinal Tract. ACS Nano. 2014; 8:4450–4464. [PubMed: 24720650]

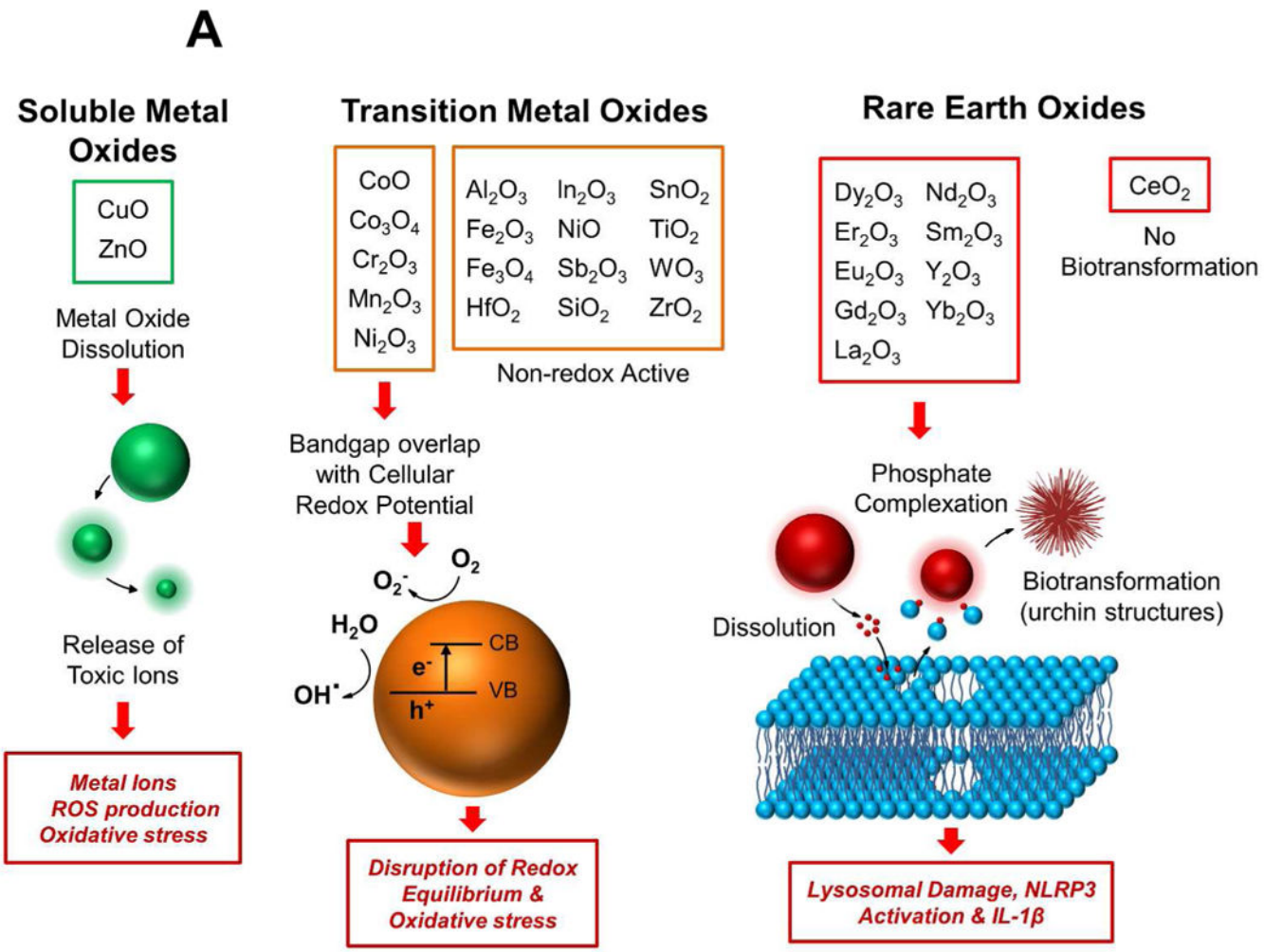

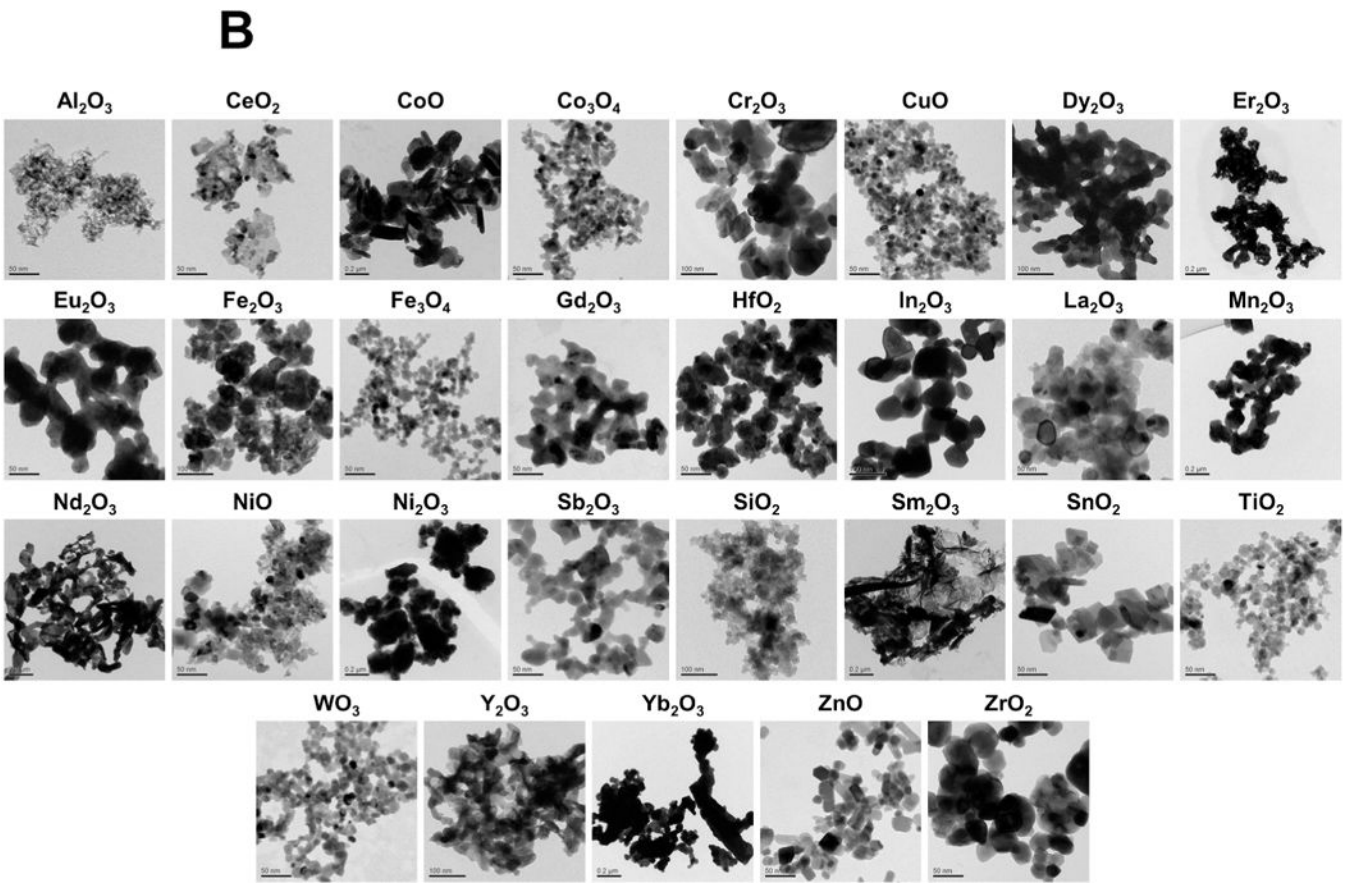

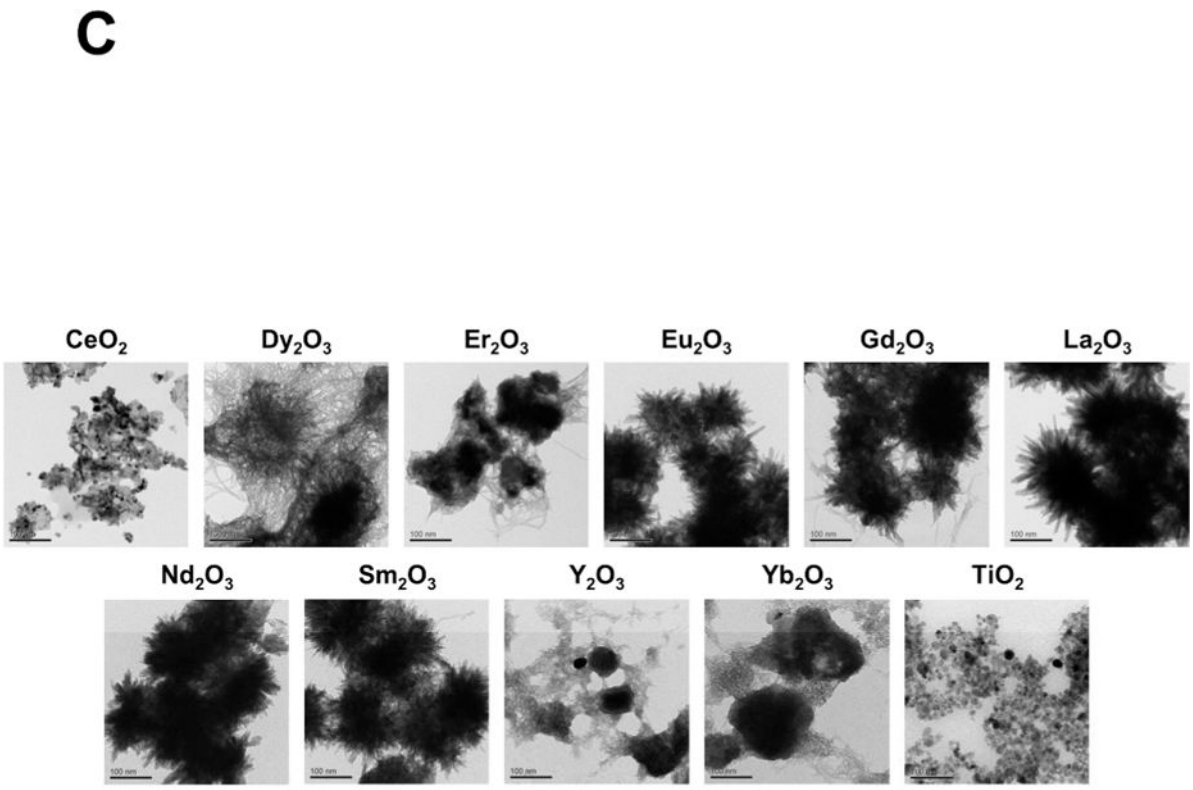

Figure 1.

Mechanistic toxicological profiling and characterization of a library of metal oxide nanoparticles including transition metal oxides (TMOs) and rare earth oxides (REOs). (A) Schematic showing the mechanisms of TMO and REO toxicity, as determined by the toxicological profiling of 24 of these materials in macrophages and the intact lung. Soluble metal oxides and redox-active TMOs induce ROS production and oxidative stress due to the release of toxic metal ions and overlap of conduction band energy with the cellular redox potential, respectively. In contrast, the lysosomal dissolution of REOs in an acidic environment, except for CeO_2 nanoparticles, leads to the release of rare earth ions that upon complexation to biological phosphates precipitate on the particle surface, leading to biotransformation into urchin-shaped structures. This triggers lysosomal damage, NLRP3 inflammasome activation, and IL-1β production. For the purposes of this study, 5 additional REOs were acquired, including Dy_2O_3, Er_2O_3, Eu_2O_3, Nd_2O_3, and Sm_2O_3. (B) Transmission electron microscopy (TEM) images of all 29 nanoparticles. The images were captured using a JEOL 1200-EX TEM with accelerating voltage of 80 kV. (C) TEM demonstrating the transformation of REOs into sea urchin structures upon abiotic exposure to phagolysosomal simulant fluid (PSF). Similar structures also form in cells (see Figure 5D,E).

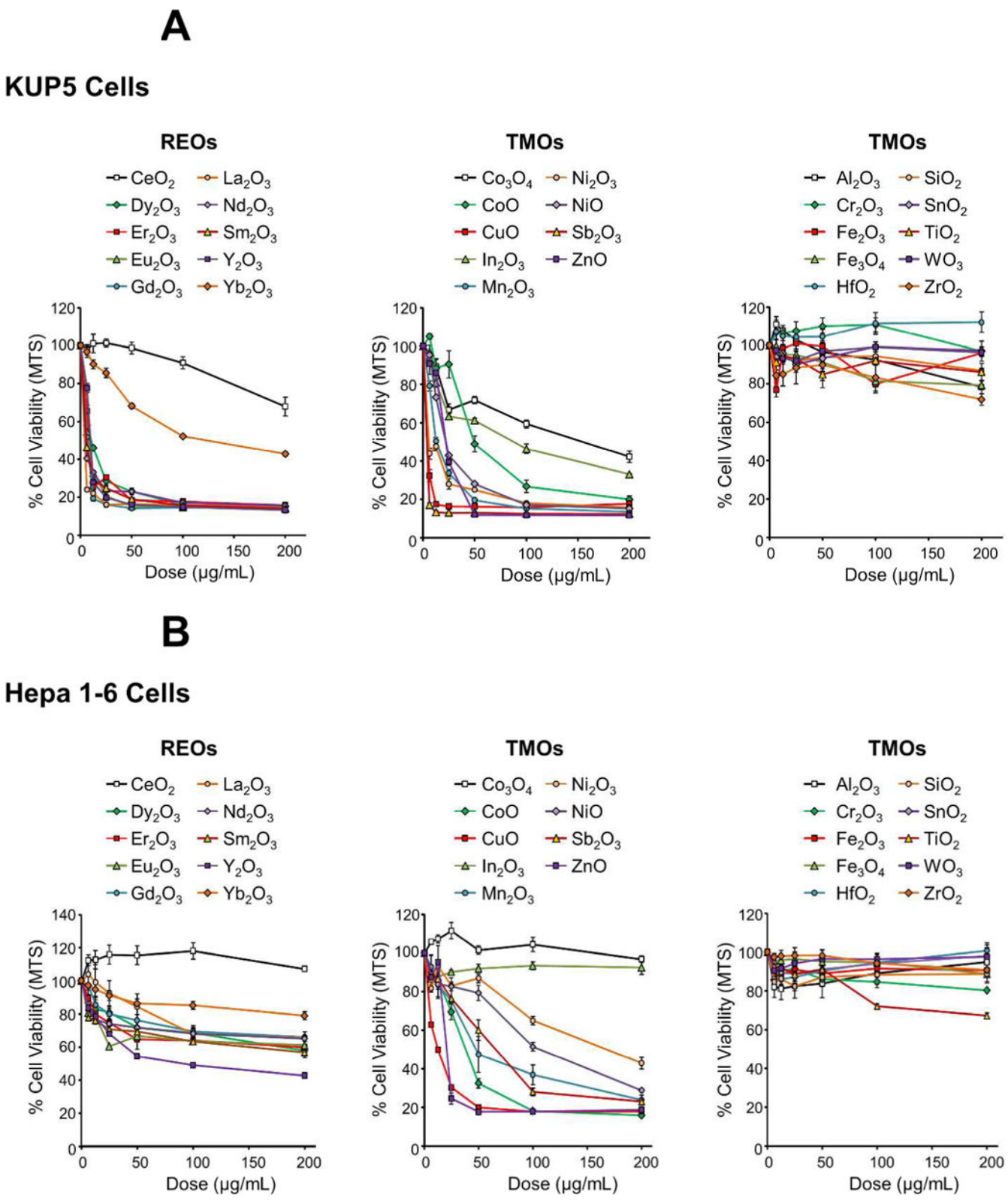

C

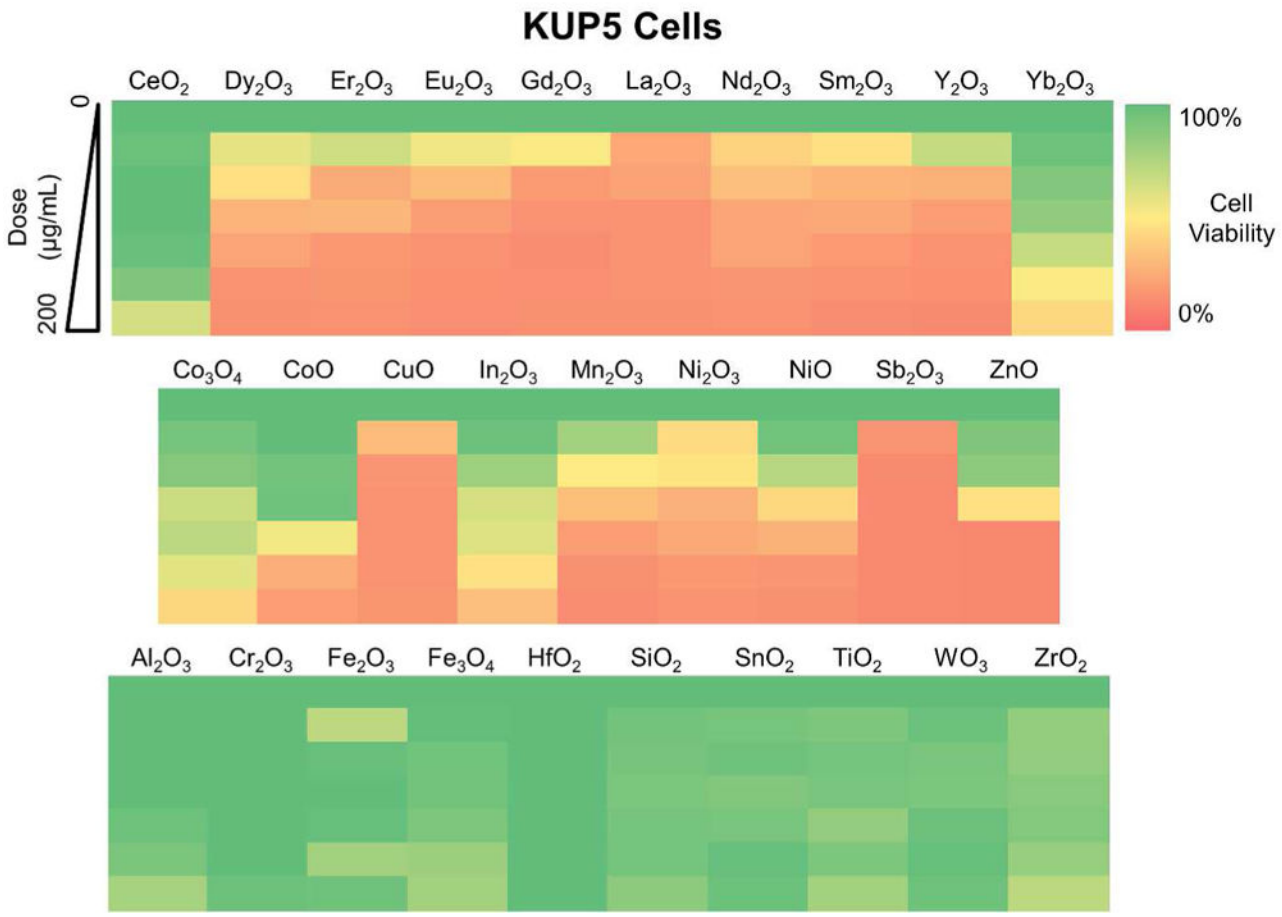

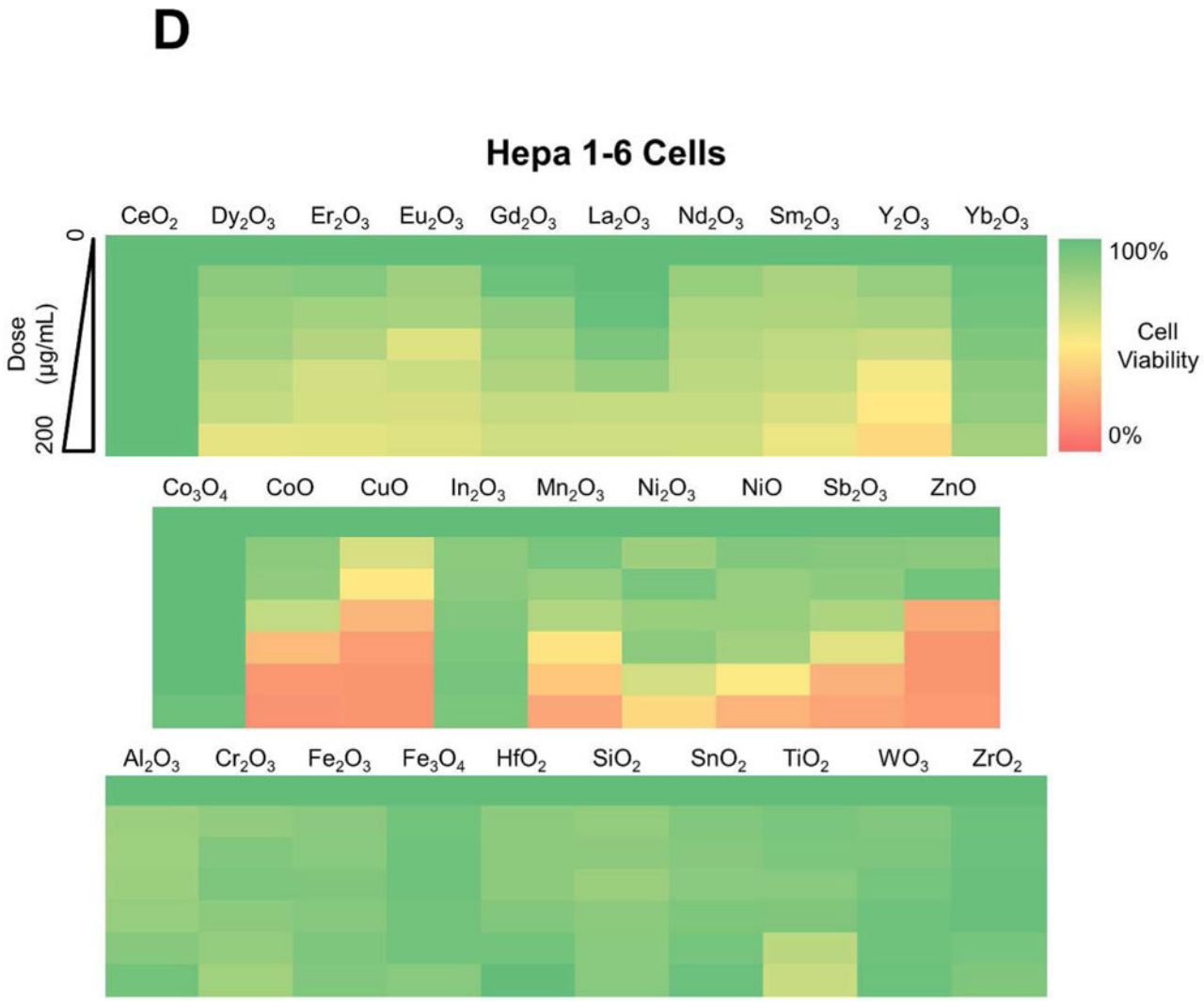

Figure 2.

Cytotoxicity screening of MOx nanoparticles in KUP5 and Hepa 1-6 cells. Use of an MTS assay to assess the viability of (A) KUP5 and (B) Hepa 1-6 cells after exposure to REO and TMO nanoparticles for 24 h over a dose range of 6.25-200 μg/mL. The results are reported in 3 material categories, namely for REOs, redox-active TMOs and inert TMOs. The viability of non-treated control cells was regarded as 100%. The results were also expressed as heat maps for (C) KUP5 and (D) Hepa 1-6 cells, calibrated against the color scale in the sidebar.

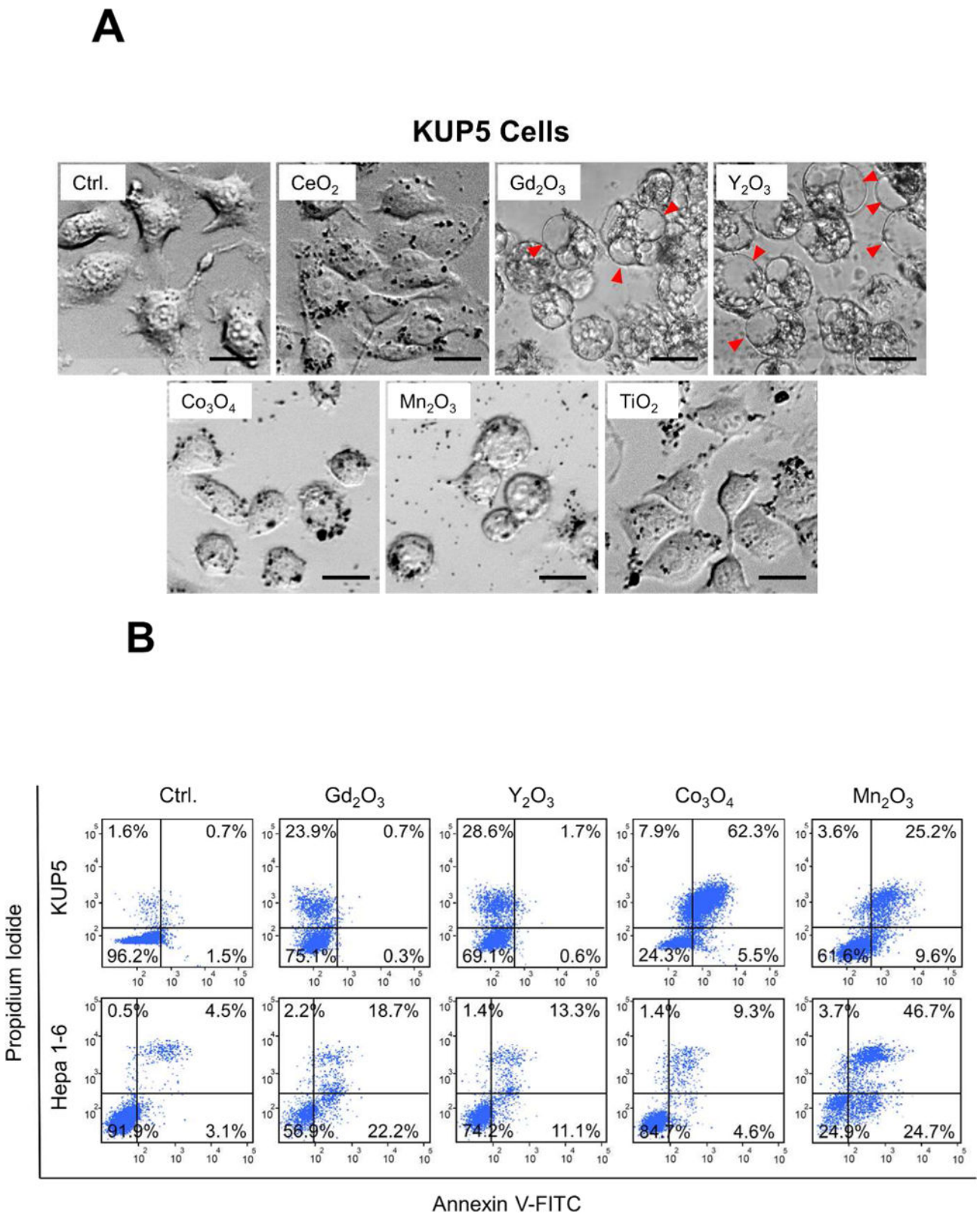

Figure 3.

REOs induce apoptotic cell death in Hepa 1-6 and non-apoptotic cell death in KUP5 cells. (A) Optical microscopy images showing the induction of cell swelling and membrane blebbing by REOs in KUP5 cells. LPS-primed (1 μg/mL, 4 h) KUP5 cells were seeded into an 8-well chamber slide and exposed to metal oxides (12.5 μg/mL) for 6 h. The red arrows point to the cellular swelling with Gd_2O_3 and Y_2O_3 nanoparticles. In contrast, CeO_2 and the TMOs did not induce swelling. The scale bar is 25 μm. (B) Flow cytometry analysis of KUP5 and Hepa 1-6 cells using dual Annexin V-FITC and PI staining. LPS-primed KUP5 and Hepa 1-6 cells (1 μg/mL, 4 h) were exposed to the chosen nanoparticles for 3 and 18 h, respectively. After washing, the cells were stained with Annexin V-FITC and PI kits as described in the methods section. We regarded dual positive cells as apoptotic, while PI-positive/Annexin V-negative cells were labeled as non-apoptotic.

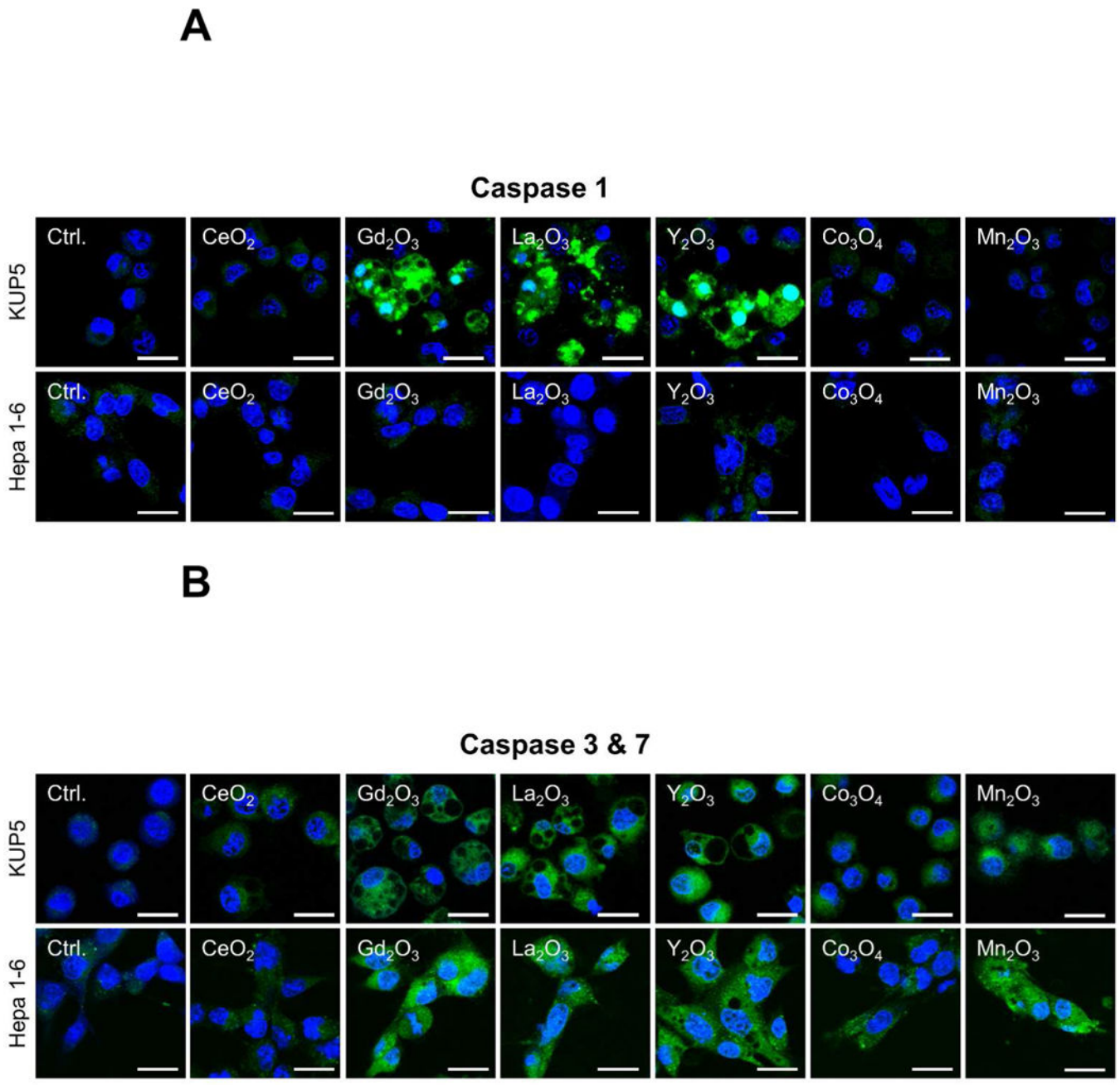

Figure 4.

Confocal microscopy images showing MOx nanoparticle-induced caspase 1 and caspases 3 and 7 expression in KUP5 and Hepa 1-6 cells. LPS-primed (1 μg/mL, 4 h) KUP5 and Hepa 1-6 cells were exposed to 50 μg/mL of the selected particles for 3 h and stained with FAM-FLICA® Caspase-1 (A) or Capase-3/7 (B) reagents for 1 h, according to the manufacturer's instructions. Cell nuclei were stained with Hoechst 33342. The scale bar is 25 μm.

A

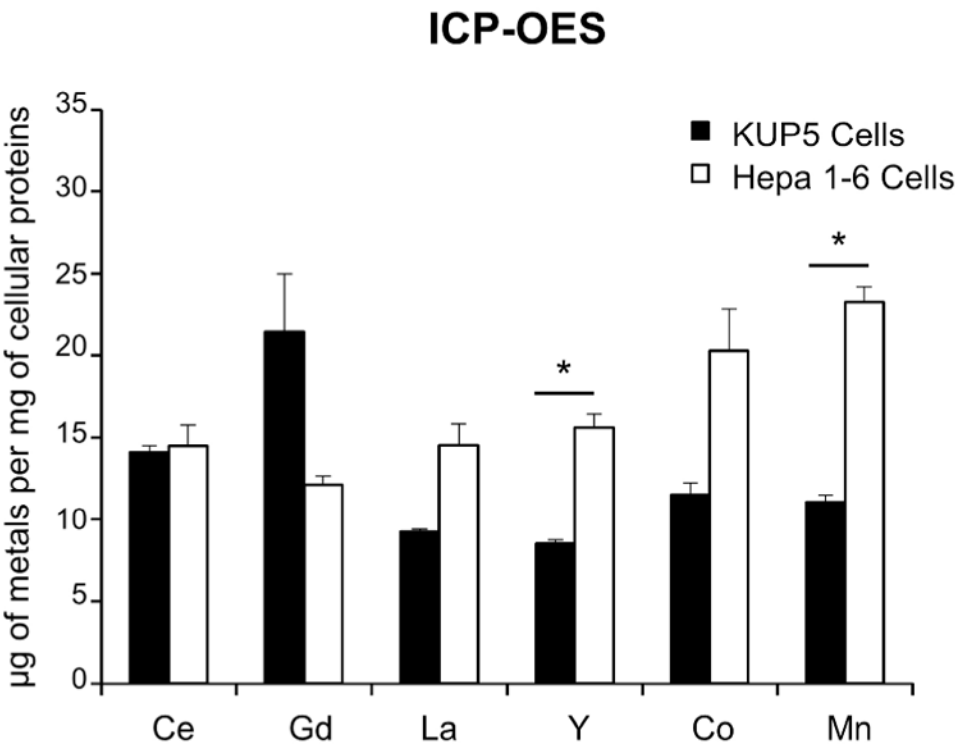

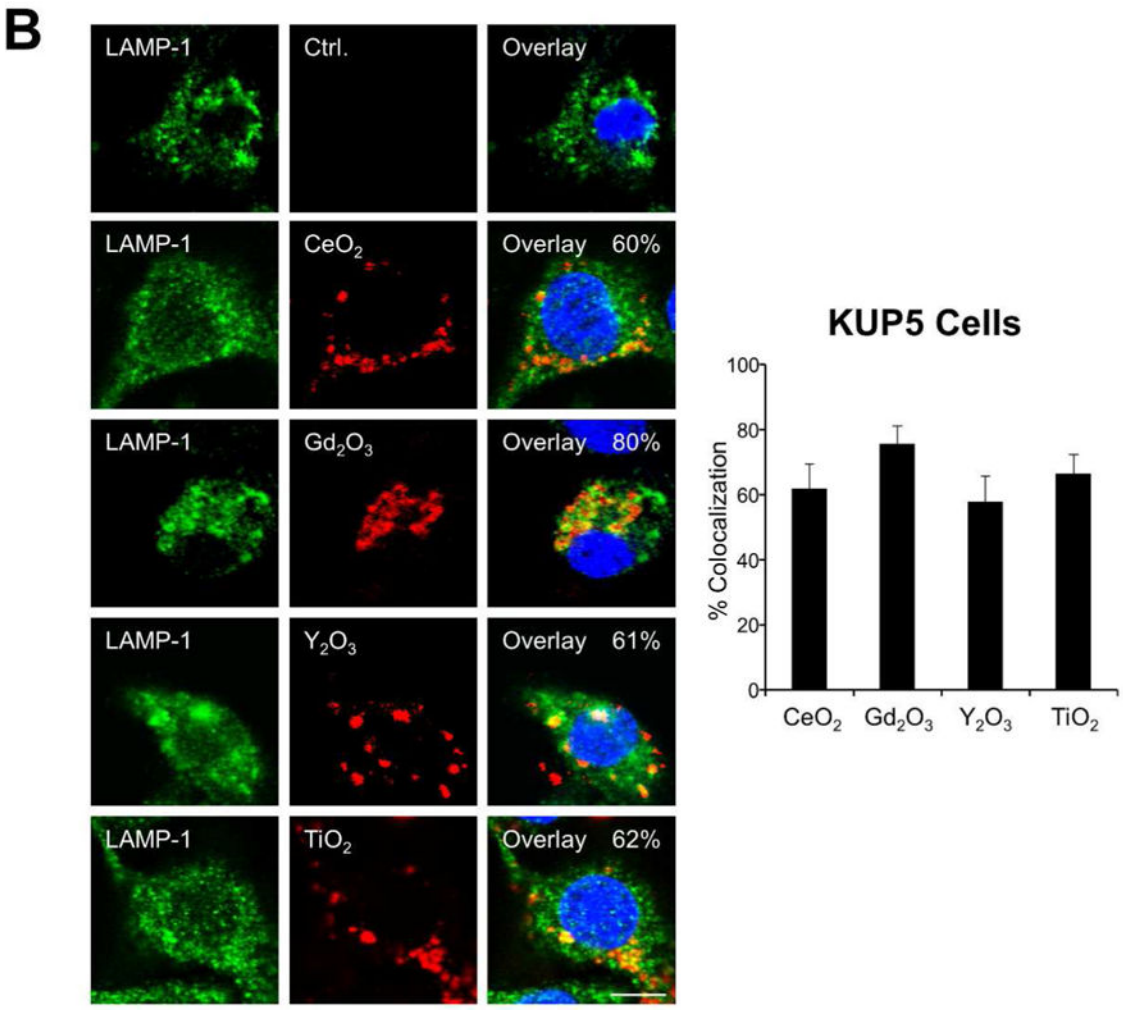

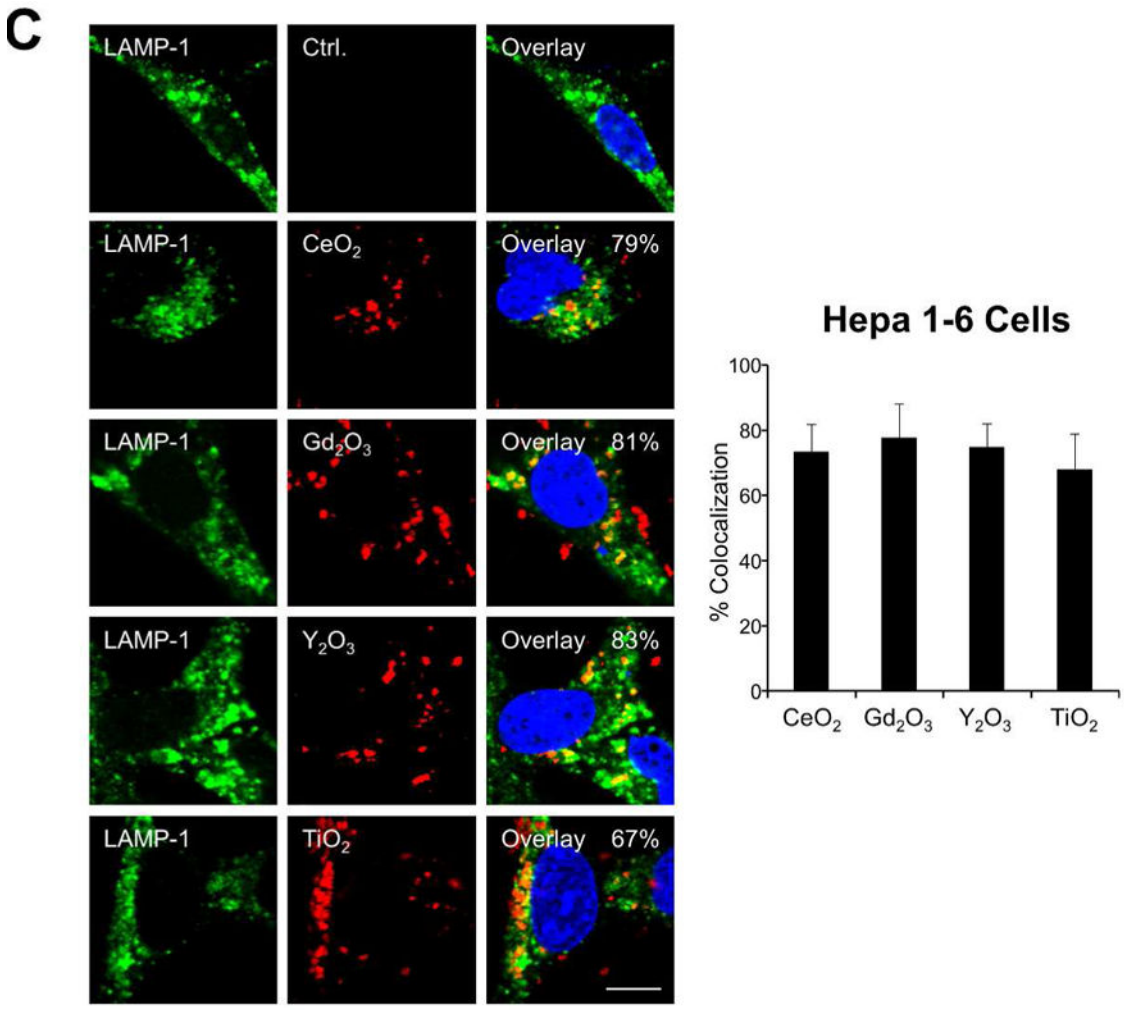

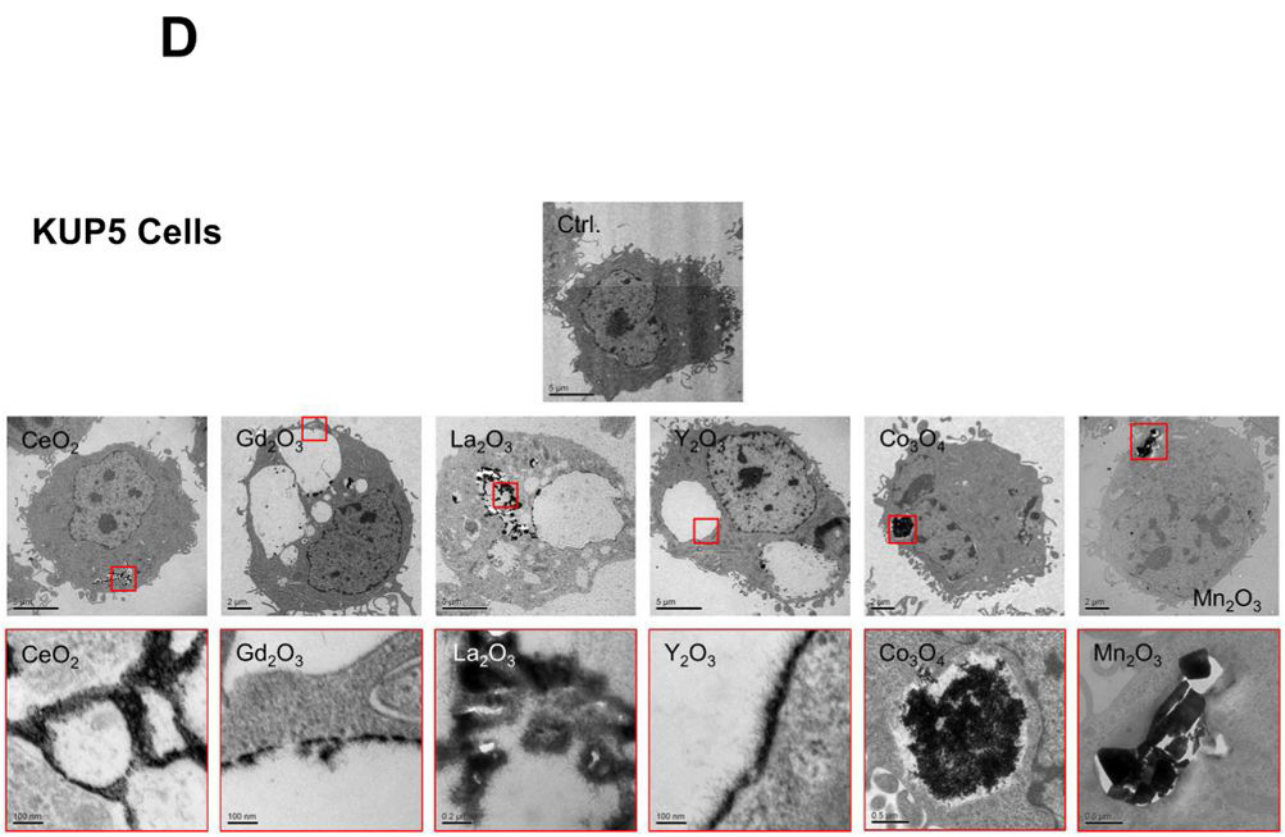

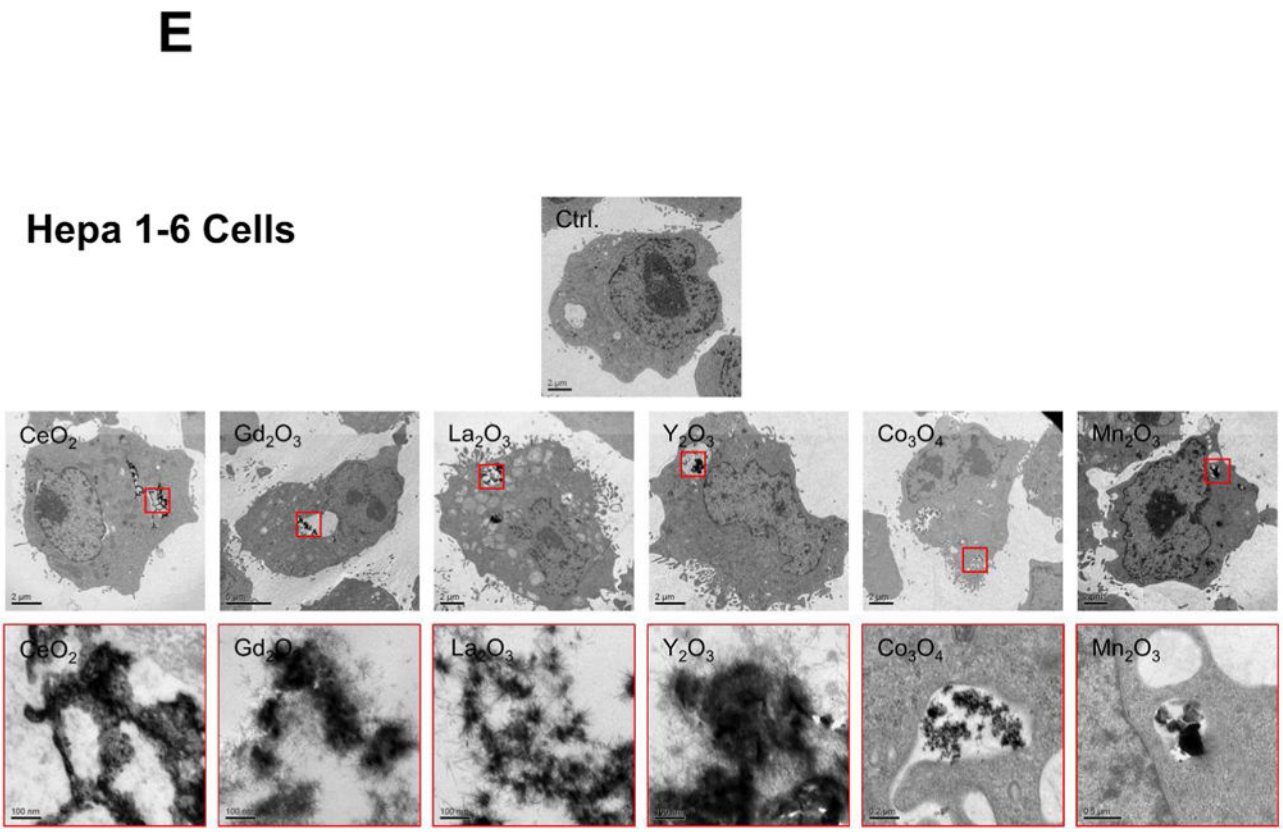

Figure 5.

Cellular uptake and subcellular localization of MOx nanoparticles. **(**A) Use of ICP-OES to quantify MOx nanoparticle uptake in KUP5 and Hepa 1-6 cells. After 4 h of treatment with 12.5 μg/mL of the selected nanoparticles, KUP5 and Hepa 1-6 cell pellets were collected and acid digested for assessment of their metal content by ICP-OES. *p<0.05 compared to KUP5 cells. (B) and (C) show confocal microscopy to assess cellular uptake and intracellular localization in lysosomes (LAMP-1 staining). DyLight 594-labeled nanoparticles (12.5 μg/mL) were incubated with KUP5 (B) and Hepa 1-6 (C) cells for 2 and 6 h, respectively. Cells were fixed, permeabilized and stained with Alexa 488-labeled LAMP-1 antibody and Hoechst 33342 for labeling of the lysosomes and nucleus, respectively. Following image acquisition with a Confocal SP8-SMD microscope, the percentages of particles co-localizing with LAMP-1 were quantified with ImageJ software. The scale bar is 10 μm. (D) and (E) show TEM micrographs of KUP5 and Hepa 1-6 cells, respectively, after treatment with 25 μg/mL MOx nanoparticles for 2 h. The images in the upper and lower panel were captured at 6000-8000× and 100000-200000× magnifications, respectively. The scale bar for each TEM micrograph is embedded in the image. Please notice the intracellular biotransformation of REOs to urchin-shaped structures in both cell types.

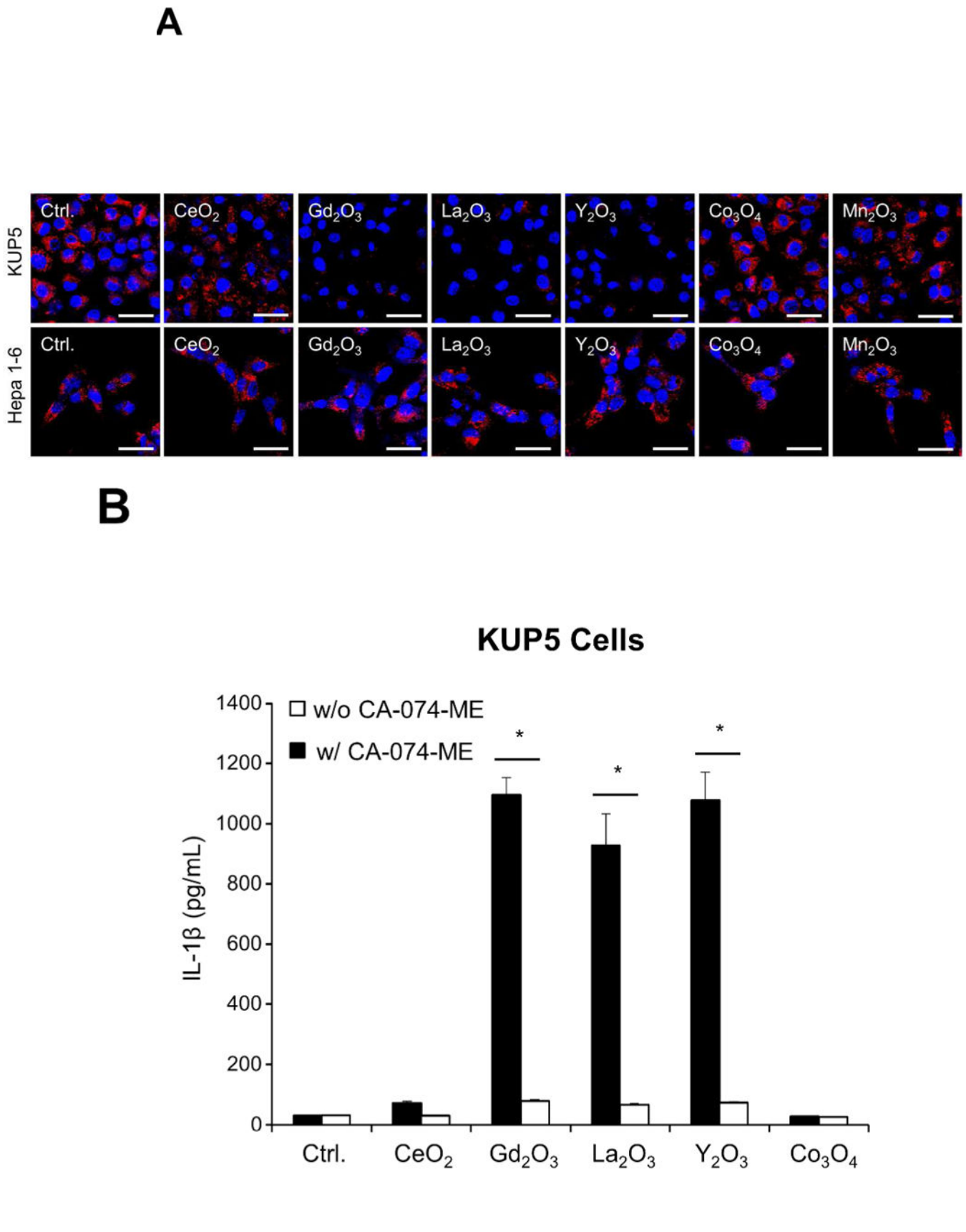

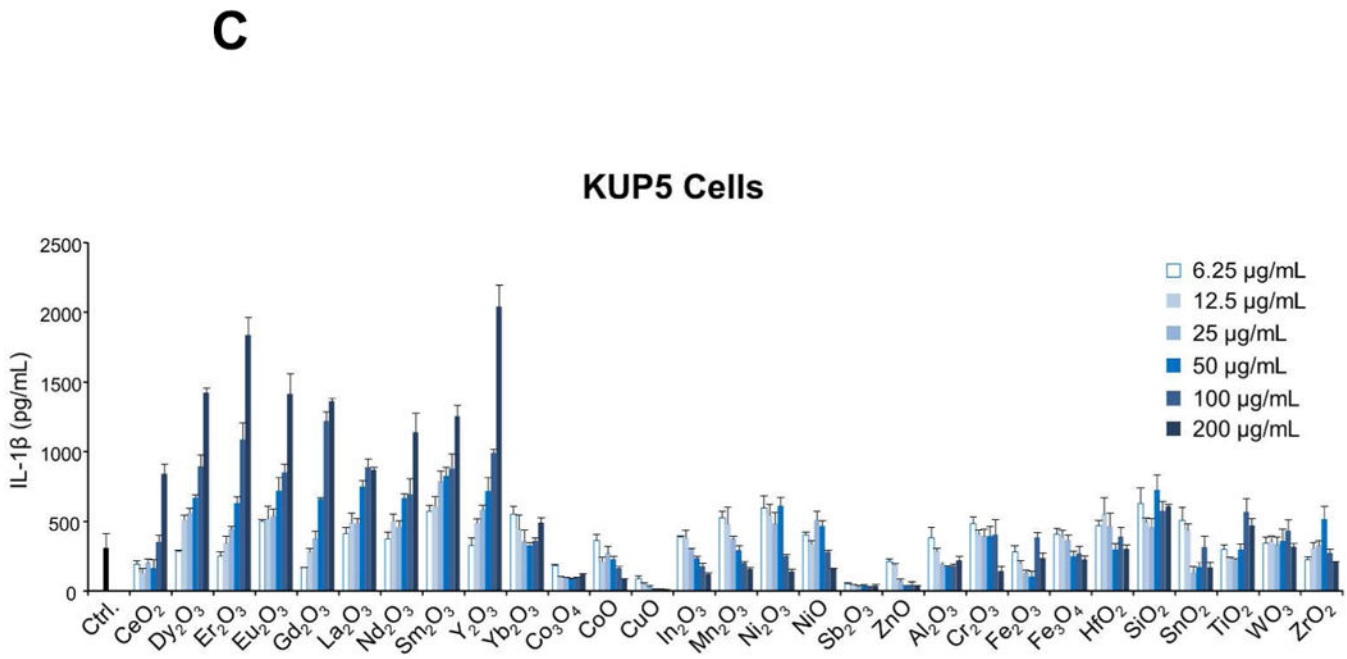

D

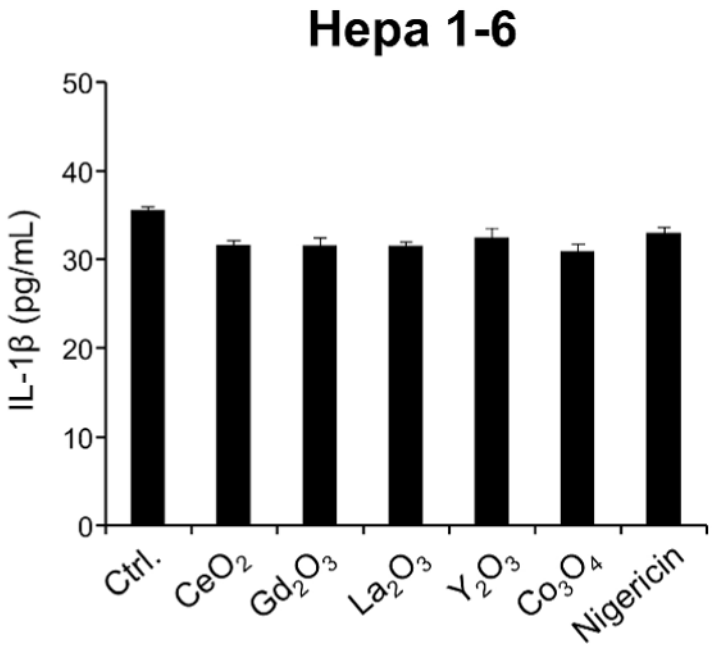

E

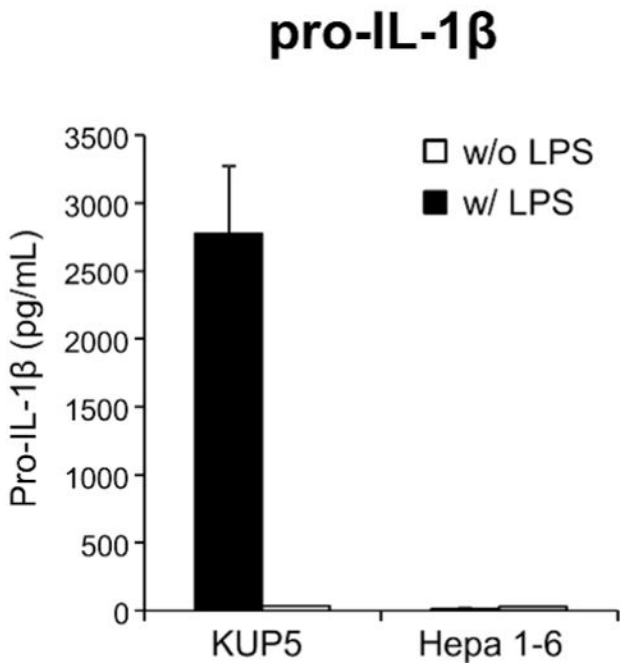

F

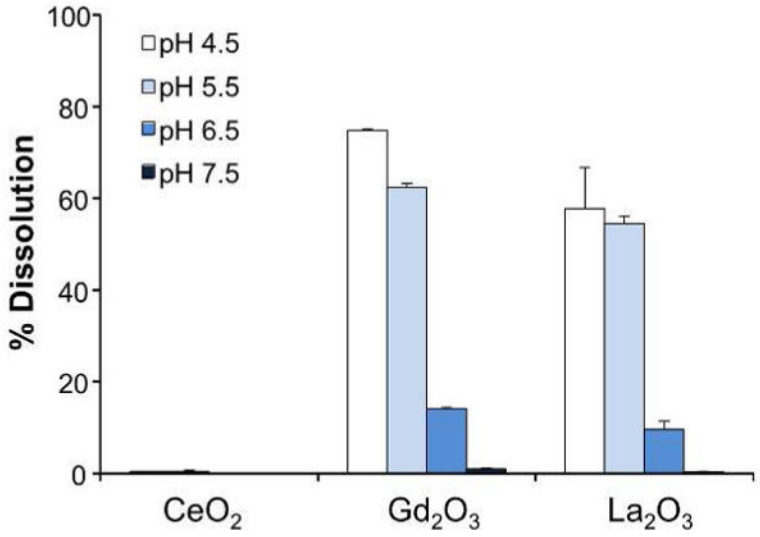

Figure 6.

Confocal microscopy to assess lysosome damage, IL-1β release and the effect of the cathepsin B inhibitor on cytokine production, induction of pro-IL-1β in LPS-primed KUP5 and Hepa 1-6 cells,. Lysosomal damage and cathepsin B release induced by REOs in KUP5 and Hepa 1-6 cells. (A) LPS-primed (1 μg/mL, 4 h) KUP5 and Hepa 1-6 cells were exposed to 50 μg/mL of the chosen nanoparticles for 1 h. Cells were stained with Magic Red-labeled cathepsin B substrate for 30 min, as well as Hoechst 33342 to reveal nuclear localization. Confocal images were acquired with a Confocal SP8-SMD microscope using DAPI and Magic Red filters. The scale bar is 40 μm. (B) LPS-primed (1 μg/mL, 4 h) KUP5 cells were exposed to 200 μg/mL of the nanoparticles in the presence of 30 μM of the cathepsin B inhibitor, CA-074-Me, for 6 h. IL-1β release in the supernatant was quantified by ELISA. *p<0.05 compared to KUP5 cells without CA-074-Me treatment. (C) Dose-dependent IL-1β release by 29 MOx nanoparticles in KUP5 cells. LPS-primed (1 μg/mL, 4 h) KUP5 cells were exposed to a wide dose range of nanoparticles (6.25-200 μg/mL) for 24 h. Supernatants were collected to measure IL-1β production by ELISA. (D) LPS-primed Hepa 1-6 cells were exposed to 100 μg/mL of the chosen nanoparticles for 24 h and IL-1β production was assessed by ELISA. Nigericin (10 μM) was used as a positive control. (E) KUP5 and Hepa 1-6 cells were treated with 1 μg/mL of LPS for 4 h. Cells were lysed to release intracellular proteins. Pro-IL-1β levels were quantified by ELISA. (F) CeO_2, Gd_2O_3, and La_2O_3

nanoparticles (100 μg/mL) were suspended in pH-adjusted MES buffers (1.5 mL) at 37 °C for 30 min. Following the centrifugation of nanoparticle suspensions (15000 rpm, 10 min), the supernatants were collected for acid digestion and their metal content was measured by ICP-OES.

A

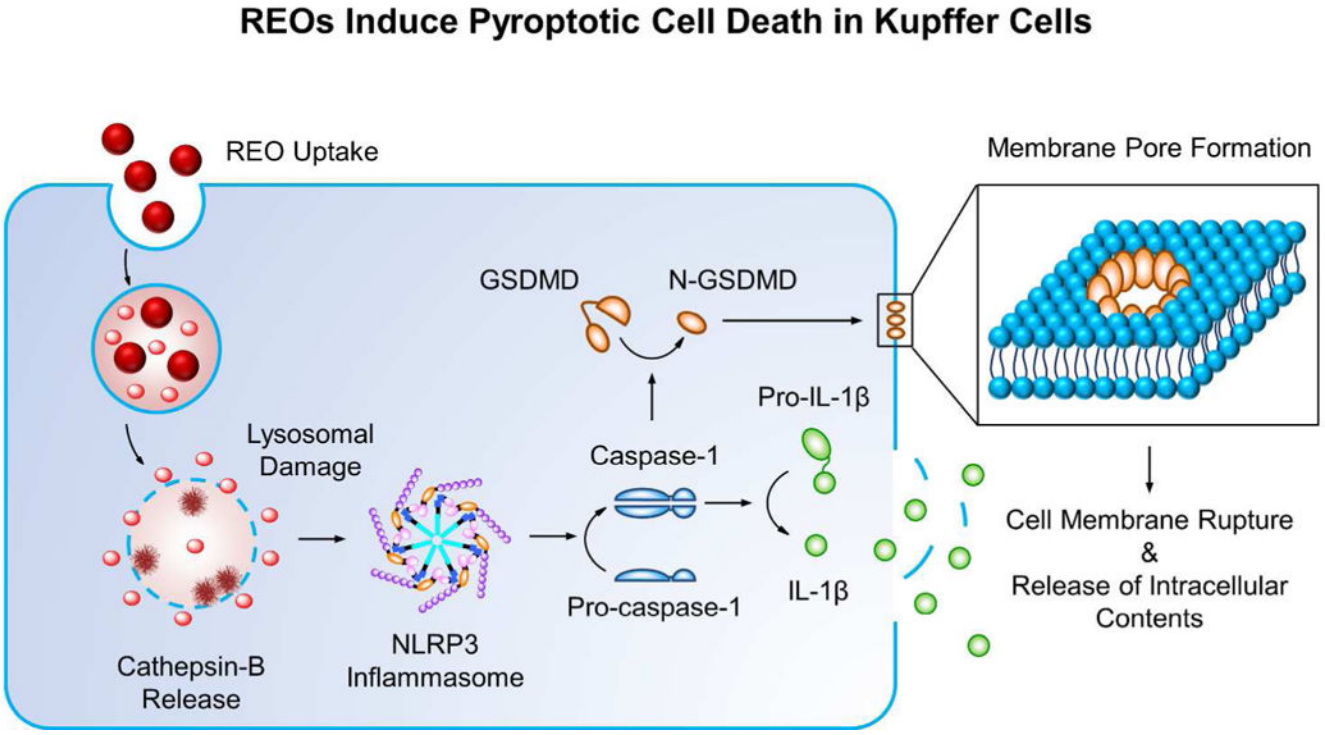

B

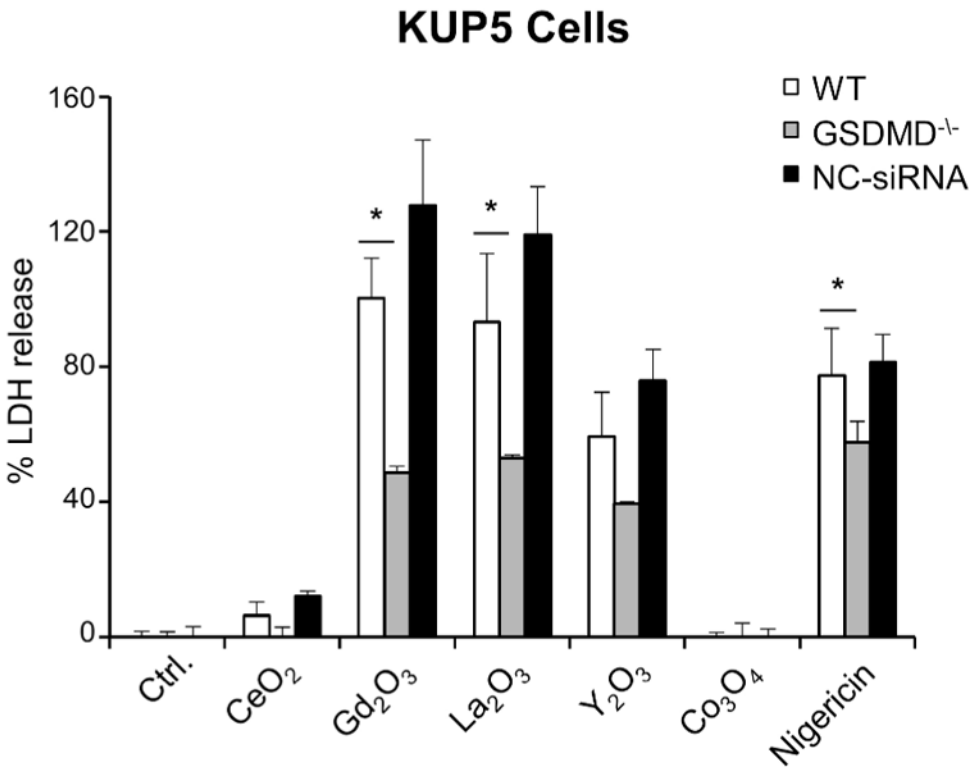

Figure 7.

Confirmation that the induction of cell death by REOs represents a pyroptosis process in Kupffer cells. (A) Schematic depicting the possible pathway by which REOs induce pyroptosis. Intralysosomal particle biotransformation leads to damage to the organelle and NLRP3 inflammasome activation. The accompanying activation of caspase 1 leads to the cleavage of pro-IL-1β, as well as gasdermin D (GSDMD), leading to the generation of a N-terminal fragment, N-GSDMD. Oligomerization of N-GSDMD in the cell membrane leads to the formation of pores, cell swelling, release of pro-inflammatory products and ultimately the features of pyroptotic cell death. (B) LDH cellular release to show that siRNA knockdown of GSDMD ameliorates REO-induced cell death in KUP5 cells. LPS-primed (1 μg/mL, 4 h) KUP5 cells were exposed to 200 μg/mL of the chosen MOx nanoparticles for 3 h. Cellular supernatants were collected to assess LDH release by a CytoTox 96® NonRadioactive Cytotoxicity (LDH) Assay kit. Nigericin (10 μM) was used as a positive control. *p<0.05 compared to particle treated wild type KUP5 cells.

A

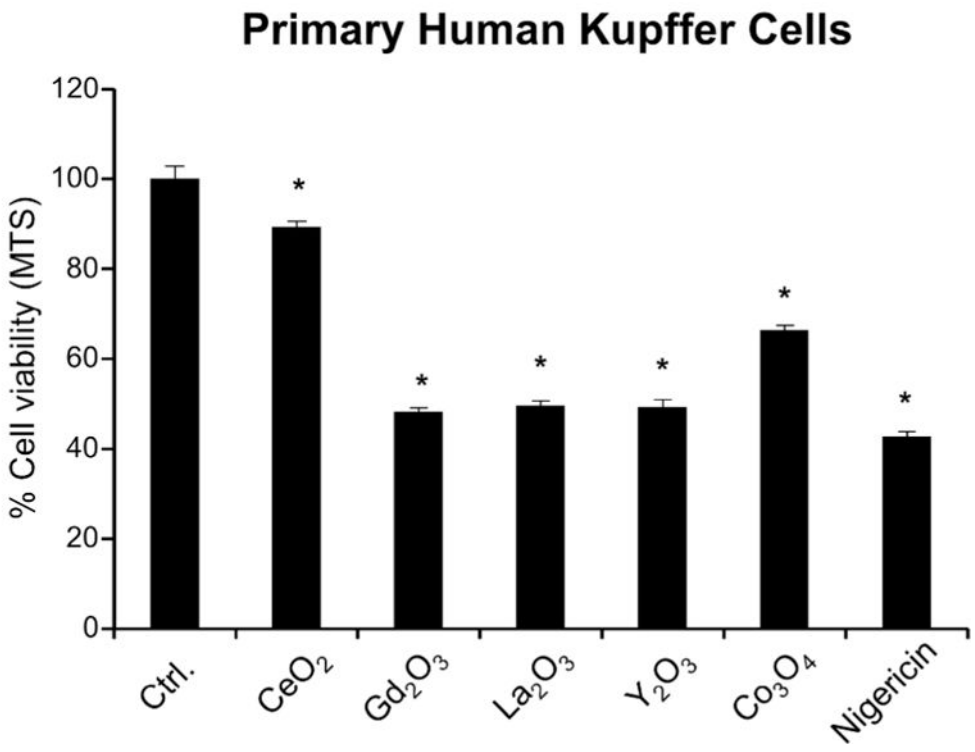

B

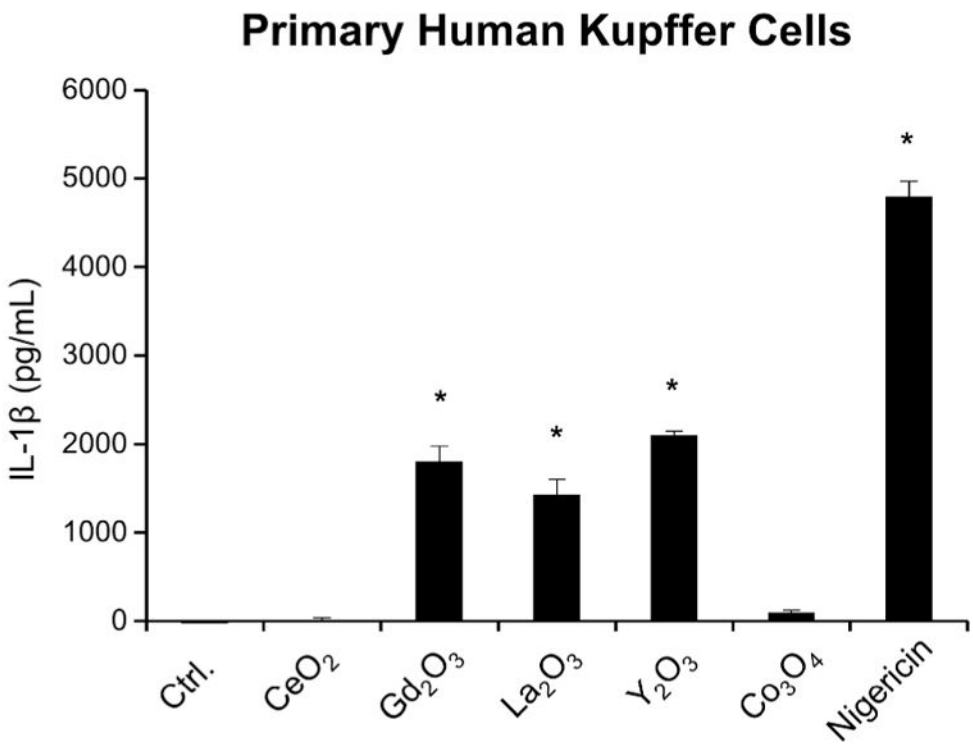

C

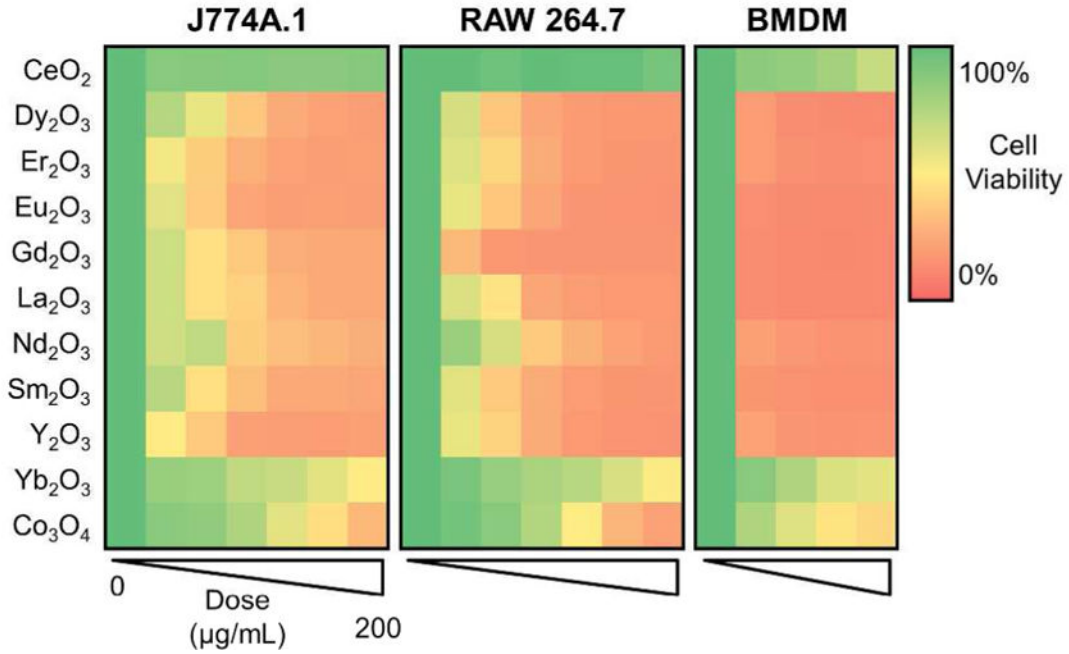

D

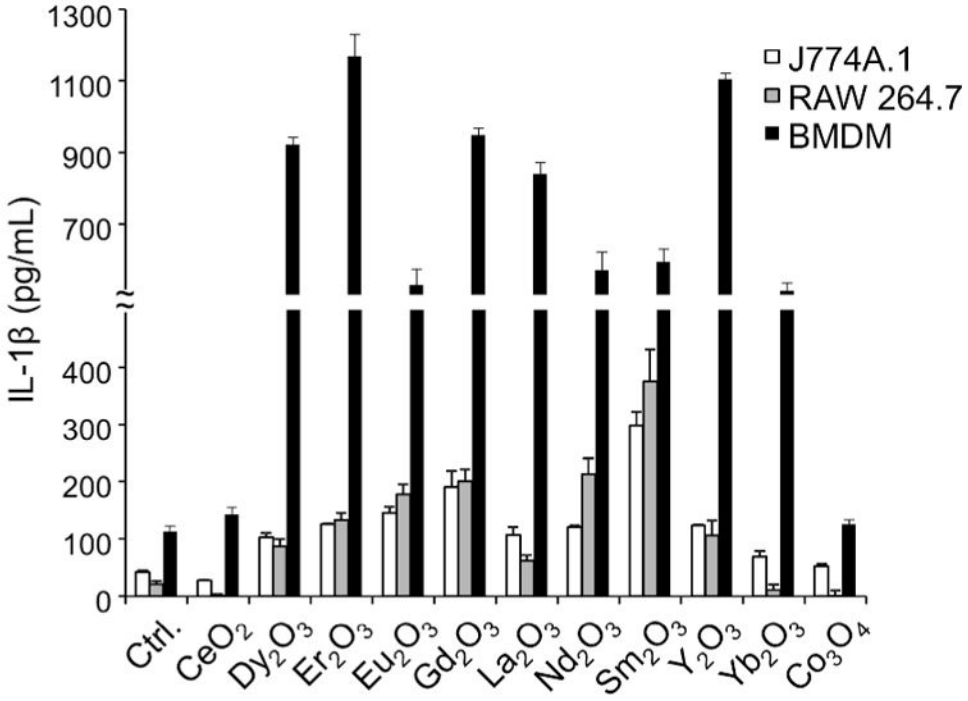

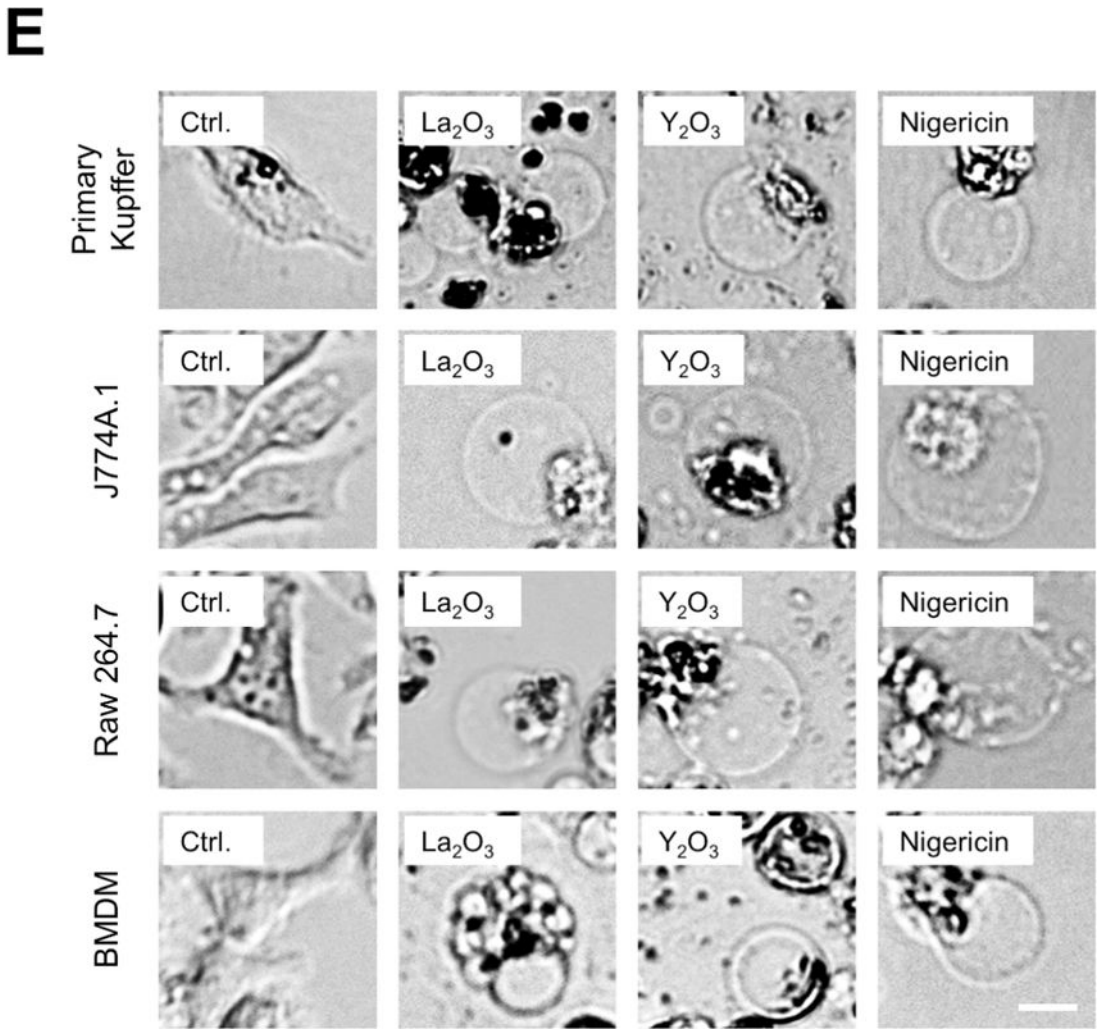

Figure 8.

REOs induce pyroptosis in primary human Kupffer cells and other phagocytic cell types. (A) LPS-primed (1 μg/mL, 4 h) primary Kupffer cells were exposed to 50 μg/mL MOx nanoparticles for 24 h, and cell viability was determined by the use of a MTS assay. Nigericin (10 μM) was used as a positive control. (B) IL-1β release in the supernatant was quantified by ELISA. (C) J774A.1, RAW 264.7 cells and BMDMs were exposed to MOx nanoparticles for 24 h. The cell viability was assessed by the MTS assay and the results reported as heat maps. (D) LPS-primed J774A, RAW 264.7 cells and BMDMs were exposed to 200 μg/mL MOx nanoparticles for 24 h and IL-1β production was quantified by ELISA. (E) Optical microscopy images showing the cell swelling and membrane blebbing in macrophages and primary KCs. The scale bar is 25 μm. *p<0.05 compared to untreated control cells.